Modification of Cerium Oxide with Different Dopants and Synthesis Methods

Master's thesis in Innovative and Sustainable Chemical Engineering

YUQI ZHANG

DEPARTMENT OF CHEMISTRY AND CHEMICAL ENGINEERING

CHALMERS UNIVERSITY OF TECHNOLOGY
Gothenburg, Sweden 2022
www.chalmers.se

Master's thesis 2022

Modification of Cerium Oxide with Different Dopants and Synthesis Methods

YUQI ZHANG

CHALMERS
UNIVERSITY OF TECHNOLOGY

Department of Chemistry and Chemical Engineering
Division of Applied Chemistry
Per-Anders Carlsson Research Group
Chalmers University of Technology
Gothenburg, Sweden 2022

Modification of Cerium Oxide with Different Dopants and Synthesis Methods
YUQI ZHANG

Supervisor: Andreas Schaefer, Chemistry and Chemical Engineering
Examiner: Per-Anders Carlsson, Chemistry and Chemical Engineering

Master's Thesis 2022
Department of Chemistry and Chemical Engineering
Division of Applied Chemistry
Per-Anders Carlsson Research Group
Chalmers University of Technology
SE-412 96 Gothenburg
Telephone +46 72 949 3969

Typeset in LaTeX
Printed by Chalmers Reproservice
Gothenburg, Sweden 2022

Modification of Cerium Oxide with Different Dopants and Synthesis Methods
YUQI ZHANG
Department of Chemistry and Chemical Engineering
Chalmers University of Technology

Abstract

Cerium oxide has many applications as a reducible oxide. In this paper, different dopants (Sm, Fe, Pt, and Rh) and synthetic methods were used to modify ceria to obtain metal-doped ceria with high specific surface area and high homogeneity. For different synthesis methods, different parameters that may have affect on the specific surface area were also investigated. The synthesized oxides were characterized employing N_2-physisorption, XRD, etc. to compare the surface area, crystal structure, and purity. The results showed that different synthesis methods have the greatest influence on the specific surface area, and the co-precipitation method is better than the citric acid method or the modified Pechini method in synthesizing oxides with high specific surface area. In the co-precipitation method, the choice of precipitant also played a role. Among the precipitants tested in this project (ammonia, urea and sodium hydroxide), sodium hydroxide performs best in getting high surface area. Citric acid and Modified Pechini method performed better in obtaining more homogeneous samples.
Two typical doped ceria synthesised by sodium hydroxide method were selected as carriers ($Ce_{0.8}Sm_{0.2}O_{1.9}$, $Ce_{0.8}Fe_{0.2}O_{1.9}$), and the catalysts were prepared by supporting metal Rh. The catalysts were characterized by N_2-physisorption and CO-chemisorption to get the information about specific surface area and metal dispersion and size. Finally, the performance of the catalysts in the CO_2 methanation reaction was tested and compared with Rh/ceria catalysts with Rh weight percentage of 1, 2, 3 wt.% and doped Rh cerium oxides with Rh content of 0.5, 2.5, 5.5 wt.%.

Keywords: Cerium Oxide, Dopant, Co-precipitation, Citric Acid Method, Modified Pechini Method, CO_2 Hydrogenation.

Acknowledgements

The research work was carried at Per-Anders Carlsson's group at the department of applied chemistry under the supervision of Dr. Andreas Schaefer and Prof. Per-Anders Carlsson.
I would first like to thank Prof. Per-Anders. When I ventured to ask him about doing a one-year thesis project at his group, he readily agreed and expressed his support. I was very grateful for the opportunity he offered me, and all the instructions he gave me.
Dr. Andreas as my supervisor has given me invaluable guidance and help. He is very careful and methodical, by his influence, I corrected some of my minor bad habits. Starting from thinking about the project topic together, I have learned a lot about what is research and how to do research. He also taught me how to understand and operate N_2-physisorption, XRD, ASAP and flow reactor, as well as analysis the data generated by those methods by Igor. I appreciate him.
I would also like to thank the other colleagues in the amazing group. Jojo, who helped me with evaluating my synthesis method, instructed me with how to run H_2-TPD. Yanyue, when I can't find a vessel for an experiment, kindly helped me lookup all over the lab and helped me borrow from other labs. Guido, helped me with acid waste treatment and always ask me about using the pump. Felix, helped both me and Linnea about preparing catalysts. Chris, trained me with using flow reactor and helped me with report lab accident. Alex, who always gave me concern when lab accident happened to me.
The final and biggest thanks I would like to give to my families, especially my parents. Without their support I won't be able to study here in Sweden. They always have my back and encourage me. I love you my amazing mother, father, and my brother!

Yuqi Zhang, Gothenburg, June 2022

List of Acronyms

Below is the list of acronyms that have been used throughout this thesis listed in appearance order in the text:

OSC	oxygen storage capacity
PROX	Preferential CO oxidation
WGS	Water-gas shift reactions
ACP	Co-precipitation with ammonia (Ammonia method)
UCP	Co-precipitation with urea (Urea method)
SCP	Co-precipitation with sodium hydroxide (Sodium hydroxide method)
CA	Citric acid method
PP	Modified Pechini method
M	General represents dopants (Sm, Fe, Pt, Rh)
IUPAC	International union of pure and applied chemistry
BET	Brunauer–Emmett–Teller
SSA	Specific surface area
STP	Standard temperature and pressure
XRD	X-ray diffraction
FWHM	Full width at half maximum (of XRD peaks)
XRF	X-ray Fluorescence Spectrometer
MFC	Mass flow controller
MS	Mass Spectrometry

Nomenclature

Below is the nomenclature of parameters, and variables that have been used throughout this thesis.

P	Actual pressure
P_0	Saturation pressure
P/P_0	Relative pressure
v	Adsorbed gas quantity
v_m	Amount of gas adsorbed in the monolayer
E_1	Heat of adsorption for the first layer
E_L	Heat of vaporization
c	BET constant
S_{BET}	BET surface area
V_m	Monolayer adsorbed gas volume
L	Avogadro's number
a	Cross-section area of adsorbed gas molecules
V	Molar volume of adsorbed gas
M	Sample mass
D_{metal}	Metal dispersion
Q_{CO}	The quantity of chemisorbed CO monolayer per gram catalyst at STP
M_{metal}	The molar mass of metal
W_{metal}	The weight percentage of active metal
F_s	Stoichiometric factor
A_{metal}	Specific active metal area
d_{metal}	The metal particle size
ρ_{metal}	Metal density
θ	Scattered angle of reflection
d	interplanar spacing
n	Wavelength integer

λ	Wavelength of the X-ray
a, b, c	Lattice constant of unit cell (Å)
α, β, γ	Lattice constant of unit cell ($\circ$)
h, k, l	Miller indices
D	Crystallite size generated from XRD
K	0.89, Scherrer constant
X_{CO_2}	Conversion of CO_2

Contents

List of Figures

List of Tables

1

Introduction

1.1 Application of metal oxides

Oxides are ubiquitous and the main components of the earth's crust and mantle are metal cations and oxygen anions. Due to the relatively ease of access to huge reserves, metal oxides are widely used in many technologies supporting environmental and human needs [1]. Among the common metal oxides one find alumina (Al_2O_3), which has the characteristics of high thermal stability, corrosion resistance, insulation properties and strength, and can be used in sapphire crystals, lithium battery separators, advanced ceramics, plasma display phosphors and so on. Another common metal oxide is silica (SiO_2) that has similar properties to alumina and is widely used in glass, construction, electronics, rubber, and other industries. These two solid oxides are also used in heterogeneous catalysts, both as catalysts and as supports for other catalytically active components in the catalysts due to their acidic surfaces, porosity, rigid framework, high specific surface area, and thermal stability [2]. Pure microporous and mesoporous Al_2O_3, SiO_2, SiO_2-Al_2O_3 as well as zeolites, which is special class of metal oxides, have all been applied in catalysts for many different reactions [3]. For example, Ni, Cu and Mo supported on Al_2O_3 or SiO_2 form catalysts that can be used in reactions related to H_2 accession for renewable hydrocarbon synthesis from vegetable oils and biomass, dry reforming of methane, CO_2 methanation [4, 5, 6], hydrodesulfurization, and ethanol steam reforming [7, 8, 9, 10]. Some noble metals (Au, Rh, Pt, Pb, Ru and Ir) supported Al_2O_3 and SiO_2 constitutes catalysts that show great activity for CO oxidation [11, 12, 13, 14, 15], methane oxidation [16, 17, 18, 19, 20, 21], fuel cracking, ammonia formation [22, 23, 24, 25], syngas production, and automotive exhaust catalysis [26, 27]. Apart from Al_2O_3 and SiO_2, other metal oxides, such as ZnO, TiO_2, ZrO_2, CeO_2, Fe_2O3, MnO_2, SnO_2, Co_3O4, CuO can also be applied in catalysis as catalyst or catalyst supports, some of them often used together as bimetallic or multimetallic oxides in order to promote catalytic activity [28, 29, 30].

Some metal oxides are strongly influenced by the reversible oxidation state of the metal, and are promising for the storage and release of oxygen, as well as in the field of catalysis, such materials can be called reducible metal oxides. In theory, all oxides can be reduced, and whether a metal oxide is a reducible oxide mainly depends on whether the necessary thermodynamic conditions required for the formation of oxygen vacancies can be achieved technically [31]. Compared with non-reducible metal oxides, reducible oxides can exchange oxygen in a relatively easy way, which are very suitable for oxidation and reduction reactions such as CO oxidation [32],

methane oxidation [33, 34, 35, 17] the water-gas shift reaction [36], and CO_2 hydrogenation [37], due to their flexible oxygen storage/release capacity and a large number of oxygen vacancies that can interact with oxygen molecules [38]. Reducible oxides can also be used as sulfur traps [39]. Many transition metal oxides belong to the category of reducible oxides, such as TiO_2, CeO_2, La_2O3, Fe_2O3, CaO, and NiO [40]. The oxygen vacancies of metal oxide can be modified by doping heteroatoms, control the morphology and dimensionality of oxide particles. For example, Yajing et al. have found that Co-doped ceria generated a much low oxygen vacancy formation energy compared with pure ceria, which leads to more abundant oxygen defects and higher reducibility [41]; MgO and ZrO_2 are considered as nonreducible oxide, while the crystal sizes of these metal oxides are reduced to nanoscale, the formation energy of an oxygen vacancy is significantly lower [40, 42].

1.2 Objective

This project focuses on the modification of ceria with different dopants (Sm, Fe, Rh and Pt) using different synthetic methods. By studying various parameters of the synthesis method, the specific synthesis steps that can generate high specific surface area, homogeneity and thermal stability are summarized. At the same time, the substitution of different dopants and the use of synthetic methods on the structural properties of ceria were analyzed, and the rules were summarized. The catalytic activity of those doped ceria were tested by supporting Rh in a flow reactor with CO_2 hydrogenation reaction.

2

Background

2.1 Cerium and cerium oxides

The rare earths is a group of seventeen elements in the periodical classification whose electronic configurations have unique properties, in the case of the so-called lanthanides (Ce $\sim$ Lu), characterized by the presence of partially filled 4f orbitals [43]. Cerium is the most abundant rare earth metal in nature, being the 25th most abundant element, which makes it more abundant than copper. Ceria has a $4f^2 5d^0 6s^2$ electron configuration (atomic number = 58), which leads to the two oxidation states of Ce^{3+} (Ce_2O_3) and Ce^{4+} (CeO_2) [44]. CeO_2, also known as ceria, plays an important role in various areas such as wastewater treatment, fuel cells, heterogeneous catalysis, gas sensors, ultraviolet absorption, glass polishing, and biomedical science owing to its easy transition between Ce^{3+} and Ce^{4+}, large oxygen storage capacity (OSC), flexible redox property and abundant oxygen vacancies [45, 46, 47, 48, 49, 50].
When used in catalysis, ceria can be encountered in different forms. Cerium oxide itself demonstrate activity in many catalytic reactions due to its unique Ce^{3+}/Ce^{4+} pairs and oxygen storage/release ability [51, 52]. In many cases, ceria is supported on different more inert materials such as SiO_2, Al_2O_3 or TiO_2 [53]. In this case, ceria often acts as an active ingredient in catalytic oxidation reactions while the inert oxides only play the role of supplying space for the catalytic reaction or dispersing ceria particles [54]. Ceria can also be used as a support, supporting metals (Pt, Pd, Rh, Au, Ni) and be applied to the elimination of undesired auto-exhaust gases, CO and soot oxidation, CO_2 conversion, and so on. Because of the excellent redox performance and appropriate surface acidity, CeO_2 can have a strong interaction with the supported metals, and supported metals considerably enhance the reducibility of ceria and its oxygen storage capacity which leads to a promotion of catalytic activity [55, 56].

2.2 Structural properties of CeO_2

The ceria has a fluorite structure, which is named after the mineral form of calcium fluoride. With four cerium atoms coordinated by eight equivalent nearest-neighbour oxygen anions in a unit cell, the cerium oxide has a face-centered unit cell (f.c.c.). The structure illustrated in fig. 2.1a [57] can be thought of as a ccp array of cerium ions with oxygens occupying all the tetrahedral holes. The nonstoichiometric CeO_2 is generally formed by the release of oxygen and the subsequent formation of oxygen

vacancy in the lattice (fig. 2.1b) [58, 56].
The transport properties of oxides, such as electrical conduction and oxygen diffusion are mainly determined by the presence, concentration and mobility of the lattice defects. These transport properties of ceria play important role in applications of solid oxide electrolytes and catalysts. Defects in ceria can be intrinsic (caused by the thermal disorder or the reaction between the solid and the atmosphere) or extrinsic (defects that formed by impurities or the introduction of aliovalent dopants) [58].
It is well known that the oxygen defects influence the optical, electrical, and mechanical properties of CeO_2, which further influence the application of ceria in catalyst [59]. To increase the number of oxygen vacancies in CeO_2 crystal structures, aliovalent dopants can be introduced into ceria lattice to modify the surface and bulk properties of cerium oxide and further stabilize the surface area and particle size. It has been found that doped caria can generate not only more oxygen vacancies but also stronger oxygen mobility and ionic conductivity.

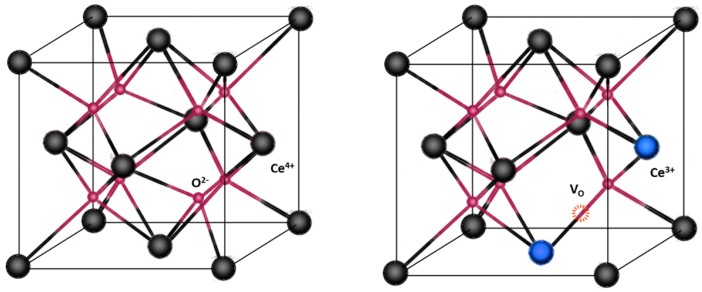

(a) **(b)**

Figure 2.1: (a) Ideal crystal structure of CeO_2; (b) Crystal structure of CeO_2 with one oxygen vacancy [57].

2.3 Modification of cerium oxides by dopants

Several cerium-cation oxide systems have been studied during the years, including isovalent dopants like Zr^{4+}, Hf^{4+} Ti^{4+} and aliovalent dopants like La^{3+}, Sm^{3+}, $Fe^{2+/3+}$, Mg^{2+}, Ca^{2+} and so on [60]. The doped composite has an effect on the oxygen storage capacity (OSC). When the Ce^{4+} is substituted by the ions lower than 4+ in valence, the changes are compensated by oxygen vacancies (such as doped Sm showed in eqn. 2.1). The crystal structure stability, the Ce^{4+}/Ce^{3+} shift and surface characteristics (i.e., surface area and porosity) usually influence the OSC of ceria and catalytic performance. As discussed in the literature, the doping of alkaline metals (Na, K, Rb, Cs etc) promoted the catalytic performance of ceria in soot oxidation by forming carbon-oxygen-metal complex [61]. The modification of alkaline earth metals like Mg, Ca, Sr and Ba on CeO_2 can improve the intrinsic activity of the catalyst supporting Ni [62]. Adding different rare-earth ions (La, Y; La, Er; La, Sm) to the CeO_2 crystal structure by co-doping method shows that oxygen defect formation was achieved by substitution of additive cations instead of Ce^{4+} in the crystal structure. The effects of defects created with different additive

types of conductivity and optical properties were observed, the total conductivity can be in the order of Sm>Y>Er [63].

$$2Sm^{3+} + CeO_2 \rightarrow 2Sm`Ce + Oxo + V...o \tag{2.1}$$

Samarium as a rare earth element has a similar property to cerium. The ionic radii of Sm is close to the critical radius value of CeO_2. This value corresponds to the ionic radius of the dopant whose substitution for the host cation causes neither expansion nor contraction of the fluorite lattice. Doping of Sm has been found to have enhanced surface area, increased oxygen mobility and higher qualities of oxygen defects [64]. Ayesha A et al. [65] found that co-doped Cu and Sm ceria catalyst presented a 64% increase in the CO oxidation activity compared to that of pristine ceria, and also discovered that Cu^{2+} and Sm^{3+} dopants were located in the nearest neighbor sites of oxygen vacancies, which reveals that doping Cu, Sm into ceria helps to generate more oxygen defects. Siakavelas et al. [66] compared a series of metal-doped Ni/$LaCeO_x$ catalysts' stability and selectivity for CO_2 methanation. The results show that the co-presence of La^{3+}, Sm^{3+}, and La^{3+}, Pr^{3+} increased the population of oxygen vacant sites, and the co-presence of La^{3+}, Pr^{3+} and La^{3+}, Mg^{3+} led to an increase of the overall basicity and plethos of moderate basic sites. Those properties helped increase the rate of CO_2 methanation reaction for Ni/La-Sm-Ce and Ni/La-Mg-Ce catalysts at low reaction temperature (300 °C). The work conducted by G. Avgouropoulos demonstrates that doping Sm^{3+} into ceria affects the dispersion of Au species on the metal oxide support, of which both large Au particles (> 10 nm) and highly dispersed gold clusters ($\sim$ 1 nm) were found on pure CeO_2, while the particle size of Au was 3.5 $\sim$ 4 nm for Sm-doped ceria. The doping of Sm benefits the catalytic performance of Au/Ceria catalyst in the preferential CO oxidation (PROX) reaction [64].

Iron is one of the most common elements on earth, the substitution of Fe in CeO_2 fluorite structure shows superior catalytic activity and brings down the cost of the catalyst considerably [67]. Fe doping has been found that can efficiently regulate the Ce^{4+}/Ce^{3+} redox couple and oxygen vacancy, which brings a higher catalytic activity and ionic conductivity. The Fe-modified Au/ceria catalyst showed an enhanced catalytic activity for CO oxidation especially at low temperatures. This is mainly because of the Ce-Fe interaction and formation of a solid solution, the close contact between both cations enhanced the reducibility of the support by generating more stable reducible species, which increases the concentration of active sites on the surface during CO oxidation reaction [68, 69]. Since the ionic radii of Fe cation is smaller than Ce^{4+}/Ce^{3+}, the incorporation of Fe usually decreases the crystallite size and lattice parameter of ceria but increases the SSA, which favors the reducibility, the number of basic sites and total conductivity [70].

Ceria-supported Pt and Rh catalysts (Pt/CeO_2, Rh/CeO_2) have been a research hot spot for a long time because of its high activity, reducibility and high oxygen storage capacity and ability of ceria to stabilize metals [71]. It has been established from previous research work that metals are usually active sites for adsorption of reactant molecules and subsequent catalysis, and these metals are usually distributed on supports in the form of metal particles [72]. However, in these catalysts, the zero-valence noble metal atoms present on the surface of metal particles as active sites

for oxidation and reduction molecules account for a small proportion (about $1/4 \sim 1/5$) of the total amount of atoms in the metal particles. If the atoms present in the metal particles can also be used, the reaction rate will theoretically be increased by 4 to 5 times. The work conducted by M.S.Hegde's group found that if precious metals are oxidized to their ions, their dispersion can be increased. These ions can be dispersed on the surface of the oxide, or directly mixed into the oxide support to form a uniform solid-phase catalyst, and in a variety of catalytic reactions (NO reduction, CO and hydrocarbon oxidation, three-way catalytic reactions, water gas shift (WGS) reactions, H_2 + O_2 recombination reactions, hydrogenation and Heck reaction) show higher activity than conventional supported metal catalysts [73]. Inspired by that, it is interesting to dope Pt or Rh into the lattice of ceria in order to improve the dispersion of noble atoms and interaction between the noble metals and CeO_2, and a higher catalytic catalyst is expected.

2.4 Synthesis methods

Synthesis and preparation methods have influence on the properties of ceria-based materials, such as crystallite phase, particle size, surface area, catalytic activities and solubility limit of dopants in ceria. There are a lot of methods reported for synthesising CeO_2 and ceria related materials.
Co-precipitation is one of the most commonly used methods for synthesising metal oxides in the light of it has the advantages of low cost, favorable industrialization, simple preparation conditions and short synthesis cycle. It can be applied to synthesising homogeneous solid solutions with two or three different metal ions [74]. Usually, the metal ions are provided by soluble metal salts (called precursors) such as the metal nitrates and metal alkoxide. The bases (ammonia, sodium hydroxide, sodium carbonate, etc.) can be used as the precipitant to help form the precipitate together with the precursors [75]. In addition, it is important that the hydroxides or precipitates form in a similar narrow pH range to have a co-precipitation (and not sequential precipitation), which is the key to obtaining homogeneous metal oxides [76]. Deshetti Jampaiah reported synthesis $Ce_{0.8}Fe_{0.2}O_x$ and $Ce_{0.8}Sm_{0.2}O_x$ with a modified co-precipitation method by using ammonia as the precipitant and metal nitrite hydroxides as precursors. The precipitations were calcined at 500 °C and 800 °C respectively. By doping Fe, Sm into ceria, the SSA was modified compared with pure ceria at both calcination temperatures (see in table 2.1). With the increase in calcination temperature, the SSA of all the metal oxides drops significantly, which mainly due to the crystallite expansion caused by sintering [77]. Not only the calcination temperature, other factors such as metal salt precursor selection, choice of precipitation agent, the pH environments and aging conditions also influence the surface area of co-precipitation method samples. The work conducted by Alfred Hagemeyer group comprehensively investigated the influence factors on generating Ce based sample with high surface area, the highest could reach 300 m^2/g by using $Ce(NO_3)_3 \cdot 6H_2O$ and NaOH as the precursor and precipitant in a rising pH environment [78]. F. lin tested the Rh-doped ceria synthesised by co-precipitation method with ammonia, the results reveals that Rh-doped ceria has an excellent structural stability since it sustains the fluorite structure even at elevated temperatures up to

1400 °C [79].

Sol-gel method is an important technique that can be used to synthesis samples with controlled structures especially ultrafine oxide materials at relatively low temperatures. It can also be applied to synthesis highly homogeneous composite with high purity [80]. "Sol" is a stable colloidal dispersion of small particles suspend in a liquid, "gel" can be formed by slowly drying "sol". In this method, some hydroxy acids such as citric, lactic, and glycolic acids are used to form polybasic acid chelates with different cations to promote uniform distribution of metal cations. O.H.Lagnna and coworkers [69] synthesised a series of Ce-Fe oxides (with Fe molar percentages of 0%, 10%, 25%, and 50%) with a sol-gel method using propionic acid as the complexing agent. The synthesised metal oxides correspond to the C- CeO_2 fluorite structure. When the molar percentage of Fe reached 25%, the phase of α - Fe_2O_3 started to show up, which means that the solubility limit of iron in the ceria matrix is 25% in their case. The fluorite structure of ceria contracted after the doping of Fe, which inline with the ionic radii of Fe and Ce. Jianqiang Wang et. al [67] used citric acid as complex agent and glycol as additive synthesised $Fe_xCe_{1-x}O_y$ solid solution with different Fe/Ce atomic ratio (1–20 mol%). The solubility of iron oxides in this case was 5 mol% according to the XRD results. The highest surface area was generated by sample $Fe_{0.03}Ce_{0.97}O_y$ (49.0 m^2/g). The doped ceria showed higher dynamic OSC and compared with the CeO_2 synthesised by the same method. Roger Jacot [81] synthesised a group of doped ceria ($M_{0.1}Ce_{0.9}O_{2-\delta}$ (M = Si, Ti, V, Cr, Zr, Nb, Rh, Hf, Ta, Nb, V, Pr, and Tb)) with Pechini-type sol-gel method, and found that the solubility of dopants in the ceria matrix tends to decrease for smaller effective ionic radii, giving rise to the formation of frequently Perovskite-related side products. The work conducted by Yunfei [82] showed that the heating process plays an important role in sol-gel method, which effects the properties of doped ceria. They compared $Sm_{0.2}Ce_{0.8}O_{1.9}$ samples synthesised by microwave-assisted sol-gel method and traditional sol-gel method with the same starting chemicals, and the microwave-assisted sol-gel method with a higher heating rate and more homogenous heating manner without thermal gradients resulted in the smaller pellet grain size and higher specific surface areas.

The Pechini method was first proposed by Maggio Pechini, which described how to use the ability of certain alpha-hydroxycarboxylic acids (such as citric, lactic, and glycolic acids) to form polybasic acid chelates with different cations to prepare films of titanate and niobate dielectrics. The chelate compound and the polyhydric alcohol solution were heated to undergo polyesterification to obtain a transparent solid resin, thereby maintaining the uniformity of cation distribution in the solution[83, 84]. The Pechini method has been modified over the years to synthesis materials with improved physical and chemical properties. The modified Pechini method has become one of the most popular synthesis methods in the low-temperature synthesis of highly pure and homogeneous substances and the development of fabrication techniques for forming certain shapes[85]. Pechini method can be applied for co-doping ceria solid solution preparation. Licurgo BorgesWinck [86] used Pechini method to dope Sm and Gd together into ceria (citric acid as complexing agent and ethylene glycol as polymerization agent, as well as ammonia hydroxide to adjust pH). The XRD results showed that both Sm and Gd were successfully sbustituted into the lattice of ceria

and confirmed a fluorite cubic phase. Others added Triton X-100 as a structure-directing agent based on the classical Pechini method, and obtained samples with higher specific surface area, higher oxygen vacancy concentration and stronger ionic conductivity than the $Ce_{0.85}Sm_{0.05}Gd_{0.1}O_{2-\delta}$ synthesized by the traditional Pechini method [87]. The Pechini method has also been used to synthesize oxides containing multiple different metals (4-6 species) due to its easy availability of homogeneous oxides. Beata Bochentyn et al. [88] successfully synthesised $Y_{0.07}Sr_{0.93}Ti_{0.8}Fe_{0.2}O_{3-\delta}$ solid solution with Pechini method, while the one synthesised by modified polymer precursor method showed impurity phases of TiO_2.

Table 2.1: Synthesis conditions and surface areas for (doped) ceria

Sample	Starting materials	Synthesis method	Calcination temperature / °C	S_{BET} / m^2g^{-1}	Ave. size / nm	Ref.
$Ce_{0.8}Fe_{0.2}O_x$	$Ce(NO_3)_3 \cdot 6H_2O$, $Fe(NO_3)_3 \cdot 9H_2O$, NH_4OH	co-precipitation	500	69	8.55	[77]
			800	12	19.01	
$Ce_{0.8}Sm_{0.2}O_x$	$Ce(NO_3)_3 \cdot 6H_2O$, $Sm(NO_3)_3 \cdot 6H_2O$, NH_4OH	co-precipitation	500	84	7.65	[77]
			800	55	25.17	
CeO_2	$Ce(NO_3)_3 \cdot 6H_2O$, NH_4OH	co-precipitation	500	41	8.92	[77]
			800	8	32.5	
$Ce_{0.95}Fe_{0.05}O_x$	$Ce(NO_3)_3 \cdot 6H_2O$, $Fe(NO_3)_3 \cdot 9H_2O$, NH_4OH	co-precipitation	600	71	9	[89]
$Ce_{0.93}Fe_{0.07}O_x$	$Ce(NO_3)_3 \cdot 6H_2O$, $Fe(NO_3)_3 \cdot 9H_2O$, NH_4OH	co-precipitation	600	40	12	[89]
$Ce_{0.9}Fe_{0.1}O_x$	$Ce(NO_3)_3 \cdot 6H_2O$, $Fe(NO_3)_3 \cdot 9H_2O$, NH_4OH	co-precipitation	600	58	8	[89]
$Ce_{0.99}Rh_{0.01}O_x$	$Ce(NO_3)_3 \cdot 6H_2O$, $Rh(NO_3)_3 \cdot 6H_2O$, NH_4OH	co-precipitation	500	-	11.8	[79]
$Ce_{0.99}Rh_{0.01}O_x$	$Ce(NO_3)_3 \cdot 6H_2O$, $Rh(NO_3)_3 \cdot xH_2O$, KOH	co-precipitation	450	145	7.9	[90]
$Ce_{0.97}Rh_{0.03}O_x$	$Ce(NO_3)_3 \cdot 6H_2O$, $Rh(NO_3)_3 \cdot xH_2O$, KOH	co-precipitation	450	138	8.7	[90]
$Fe_{0.01}Ce_{0.99}O_y$	$Ce(NO_3)_3 \cdot 6H_2O$,	sol-gel	300 (0.5h) and 500 (5h)	33.7	-	[67]
$Fe_{0.03}Ce_{0.97}O_y$	$Fe(NO_3)_3 \cdot 9H_2O$,			49.0	-	
$Fe_{0.05}Ce_{0.95}O_y$	citric acid,			42.3	-	
$Fe_{0.07}Ce_{0.93}O_y$	glycol			34.4	-	
$Sm_{0.2}Ce_{0.8}O_{1.9}$	Sm_2O_3 + HNO_3 $Ce(NO_3)_3 \cdot 6H_2O$ EDTA–NH_3 $\cdot H_2O$ NH_4OH (adjust pH to 10)	sol-gel	900	15.1	56	[82]
2wt%Pd/$Ce_{0.9}Sm_{0.1}O_{1.95}$	$Ce(NO_3)_3 \cdot 6H_2O$ $Sm(NO_3)_3 \cdot 6H_2O$ $Pd(NO_3)_2 \cdot 6H_2O$ citric acid	sol-gel	500	69.4	8.3	[91]
2wt%Pd/$Ce_{0.8}Sm_{0.2}O_{1.9}$	$Ce(NO_3)_3 \cdot 6H_2O$ $Sm(NO_3)_3 \cdot 6H_2O$ $Pd(NO_3)_2 \cdot 6H_2O$ citric acid	sol-gel	500	66.5	7.8	[91]
$Rh_{0.1}Ce_{0.9}O_x$	Rh(ii) acetate $Ce(NO_3)_3 \cdot 6H_2O$ citric acid	sol-gel	1100	-	-	[81]
$Ce_{0.8}Sm_{0.2}O_{1.9}$	$Ce(NO_3)_3 \cdot 6H_2O$ $Sm(NO_3)_3 \cdot 6H_2O$ citric acid ethylene glycol NH_4OH (adjust pH to 9)	Pechini	600	-	28.62	[86]
$Ce_{0.8}Sm_{0.15}Gd_{0.05}O_{1.9}$	$Ce(NO_3)_3 \cdot 6H_2O$ $Sm(NO_3)_3 \cdot 6H_2O$ $Gd(NO_3)_3 \cdot 6H_2O$ citric acid ethylene glycol NH_4OH (adjust pH to 9)	Pechini	600	-	31.13	[86]
$Ce_{0.8}Sm_{0.1}Gd_{0.1}O_{1.9}$	$Ce(NO_3)_3 \cdot 6H_2O$ $Sm(NO_3)_3 \cdot 6H_2O$ $Gd(NO_3)_3 \cdot 6H_2O$ citric acid ethylene glycol NH_4OH (adjust pH to 9)	Pechini	600	-	33.86	[86]
$Ce_{0.85}Sm_{0.05}Gd_{0.1}O_{2-\delta}$	$Ce(NO_3)_3 \cdot 6H_2O$ $Sm(NO_3)_3 \cdot 6H_2O$ $Gd(NO_3)_3 \cdot 6H_2O$ citric acid ethylene glycol	Pechini	550	66	12.62	[87]
$Ce_{0.85}Sm_{0.05}Gd_{0.1}O_{2-\delta}$	$Ce(NO_3)_3 \cdot 6H_2O$ $Sm(NO_3)_3 \cdot 6H_2O$ $Gd(NO_3)_3 \cdot 6H_2O$ citric acid ethylene glycol Triton X-100	Modified Pechini	550	91	9.11	[87]

3
Methodology

3.1 Synthesis of metal oxides

To generate the metal oxides with high surface areas, phase purity, and thermal stability, five synthesis methods were investigated in this project. According to the mechanisms those methods were classified into co-precipitation and gel and polymeric precursor methods. Three different precipitants: NH_4OH, urea and NaOH were investigated in the co-precipitation methods, and the synthesis processes were adjusted according to the properties of the precipitants. Gel and polymeric precursor method is the general designation of citric acid and modified Pechini method in this project. Both of them have the step of heating and evaporating the solution containing metal ions and complexing agent or polymerization agent to obtain gel or polymer. This kind of method mainly involves the reaction between mixed cations with citric acid, cations cross-linkage with the help of ethylene glycol for the polyesterization process (modified Pechini method), heating and evaporating of the solution to obtain the gel or polymeric precursor, and decomposition of the precursor material to obtain an oxide powder [85, 92].
The synthetic sample name consists of the element, the synthesis method, and the calcination temperature. For example, C80SO-ACP-F500 is expressed as a $Ce_{0.8}Sm_{0.2}O_{1.9}$ sample obtained by ammonia method calcining synthesized at 500 °C. Other dopants, Fe, Rh, and Pt are represented as F, R, and P in the sample name.

3.1.1 Co-precipitation methods

Ammonia method

For this co-precipitation method, ammonia played the role of precipitant as it includes no other metal ions and is easy to be washed away by filtering. Metal nitrates were used as the precursors. In the process of gradually adding a 2 M ammonia to the precursor solution, the pH increased continuously and was accompanied by the formation of precipitates (usually metal hydroxides). When the pH of the mixture reached 10, the adding of ammonia was stopped during continuous stirring. Then the product was left for around 45-60 min until the liquid and solid phases separated nicely, followed by filtration, washing, freeze drying for 2 days and calcined at 500 °C for 5 h (heating rate: 4 °C/min), the final product was obtained. Fig. 3.1

represents the basic steps of this method.

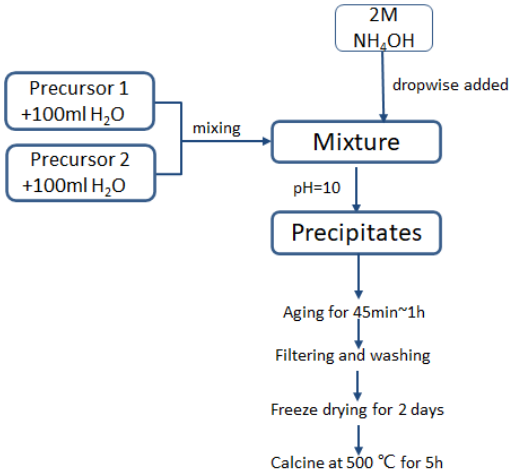

Figure 3.1: The basic process of ammonia method

Urea method

This method is based on that urea can be decomposed into cyanate and ammonium ions when increasing the temperature, and the obtained cyanate ion will further undergo conversion to carbonate and ammonium, the carbonate ions will combine together with the cations offered by precursors and form metal carbonate precipitates[93, 94]. However, for some easily hydrolyzed ions such as iron, the metal carbonates will eventually turn to metal hydroxide precipitate in the mixture.
As shown in Fig. 3.2, the precursors were separately dissolved in 50 ml Milli Q H_2O, and urea was dissolved in 100 ml Milli Q H_2O. After mixing the precursors with urea solution, the mixture was heated up to 91 °C accompanied with reflux for 15 h to decompose urea and generate precipitates. Followed by aging, filtering and washing, the precipitates were dried in the oven at 100 °C for 10 h. Then the samples were calcined at 350 °C and 500 °C to compare the effects of calcination temperature on metal oxide properties.

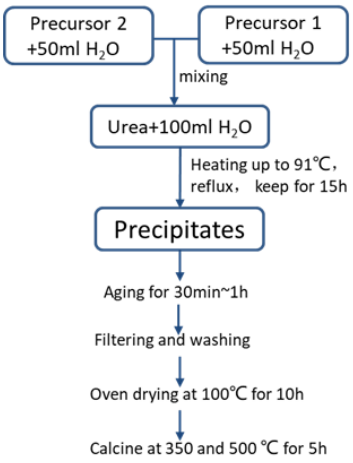

Figure 3.2: The basic process of urea method

Sodium hydroxide method

This is a co-precipitation method from a patent (US5993762A) of Johnson Matthey PLC [95]. In this method (Fig. 3.3), sodium hydroxide was used as a precipitant. The precursors were dissolved together in 20 ml Milli Q H_2O while NaOH was dissolved in 240 ml Milli Q H_2O. The NaOH solution was heated and to boiling, the precursors were slowly dropped into the boiling NaOH solution. This process should last for at least one hour. After the dropping process, the mixture was boiled at 100°C for one more hour, after which the heating and stirring were stopped. The obtained substance was cooled down and separated nicely into solid and liquid phases in the flask. Followed by filtering, washing, drying in the oven at 110 °C for 12 h and calcination at 350 °C, 500 °C, whereafter the final metal oxides were obtained.

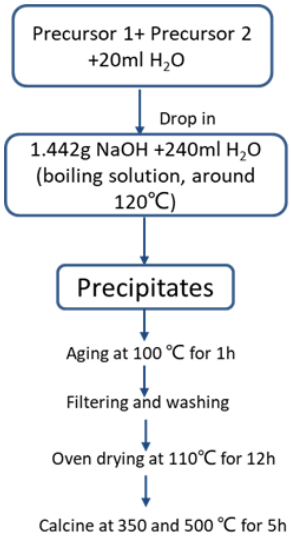

Figure 3.3: The basic process of sodium hydroxide method

3.1.2 Gel and polymeric precursor methods

Citric acid method

In this method, citric acid was used as a complexing agent, which would lead to a nice separation and mixing of the metal ions in solution. The precursors were first dissolved in a certain amount of Milli Q H_2O to generate the same concentration, and citric acid was also dissolved in water. The molar ratio between metal ions, citric acid and the water used to solve citric acid was: 1:3:40. The well-mixed citric acid and precursor solution was then heated up slowly to evaporate the solvent in the solution and get a gel-like substance (in certain cases foaming can occur during the evaporation process). The substance should mainly be the complex of citric acid

and metal ions, but it also contains NO_3^- provided by metal nitrate precursors. Followed by drying at 201 °C for 5 h and pyrolysis at 250 °C for 5 h (heating rate: 4 °C/min), citric acid and other impurity ions will be burnt away, after calcined at 500 °C for 5 h, a pure $CeMO_x$ sample was generated.

In this method, some parameters are investigated based on the BET surface areas, such as pH, condensing rate and temperatures, drying rate and temperatures, pyrolysis temperatures and calcination temperature. According to literature [84], the mixture pH affects complexing behavior between citric acid and metal ions, with the increase of pH, the chelate formed in the mixture will be more stable. Also from the pre-synthesis and characterization results of some samples, the pH seems to affect the surface area of metal oxide. Two different pH (1 and 7) are chosen in this project according to the three citric acid pKa values of 3.13, 4.76 and 6.39. At pH=1, only one carboxylic acid group is assumed to be deprotonated, while at pH=7 all three carboxylic acid groups of citric acid are deprotonated. The basic process of this method is shown in the following figure 3.4

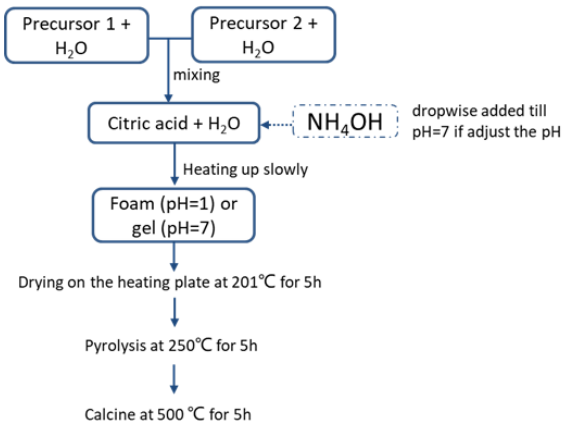

Figure 3.4: The basic process of citric acid method

Fig. 3.5 showed one type of complexing reaction between citric acid and metal cations [96]. Fig. 3.6 is an illustration of the reaction between citric acid and metal ions [84].

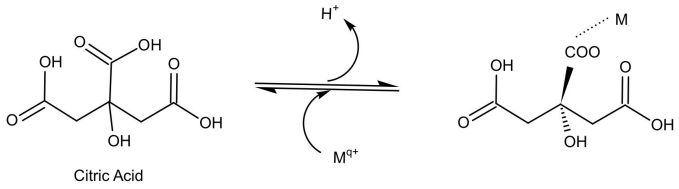

Figure 3.5: Complexing reaction between citric acid and metal ions [96].

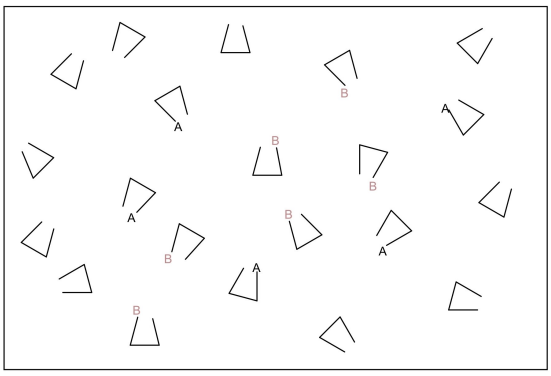

Figure 3.6: Illustration of complexing reaction between citric acid and metal ions. (A, B represent different metal ions, open triangle represents citric acid) [84].

Modified Pechini method

In this method, citric acid plays a role of complexing agent, while ethylene glycol is the polymerization agent. This method is similar to the citric acid method. In addition to adding the complexing agent citric acid to uniformly disperse the metal ions, ethylene glycol was added to undergo polyesterification. The molar ratio between metal ions, citric acid, ethylene glycol and the water used to solve citric acid was: 1:3:3:40. Then the mixture was heated to over 100 °C to allow the polyesterization between citric acid and ethylene glycol, which formed large, cross-linked networks and removal of excess water, a foam was obtained after that. Set the temperature of the heating plate to 201 °C for 5 h to dry the foam, and then put the substance into the calcine oven for pyrolysis at 250 °C for 5 h with a heating rate of 4 °C/min from room temperature, after that the carbon chains connecting the metal ions were usually eliminated. The final products were obtained after calcining at 500 °C for 5 h (heating rate: 4 °C/min)
Fig. 3.8 shows the basic reaction of the modified Pechini method [96]. Fig. 3.9 shows the complexing and polyesterization process [84].

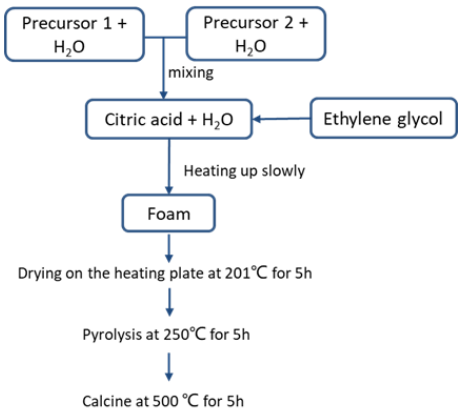

Figure 3.7: The basic process of modified Pechini method.

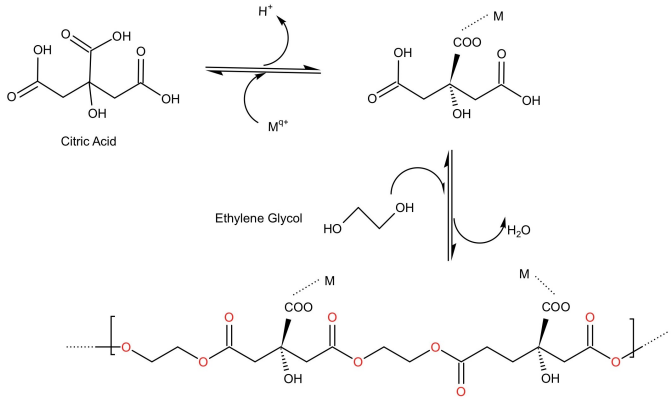

Figure 3.8: Complexing reaction between citric acid and metal ions and polyesterization between citric acid and ethylene glycol [96].

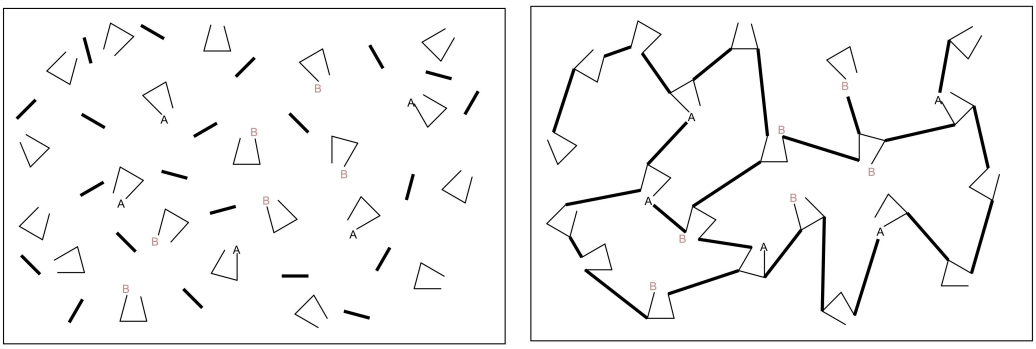

Figure 3.9: Illustration of complexing and polyesterization processes. (A, B represent different metal ions, open triangles represent citric acid, short lines represent ethylene glycol) [84].

3.2 Synthesis of metal oxide-based catalysts

The supported rhodium/$CeMO_2$ (M = Sm, Fe) catalysts were prepared by the dry impregnation method. The rhodium nitrate precursor was dissolved in the same volume of Milli Q H_2O as the pore volume and dropped into the support materials (the pore volume was obtained by dripping water into the support material and measuring the weight of water that the material can just fully absorb). Stir the mixture gently to ensure that the supports were fully soaked in the solution. Followed by free drying, calcination (5 °C/min, keep at 500 °C for 1 h), the impregnated Rh/$CeMO_2$ catalysts were obtained.

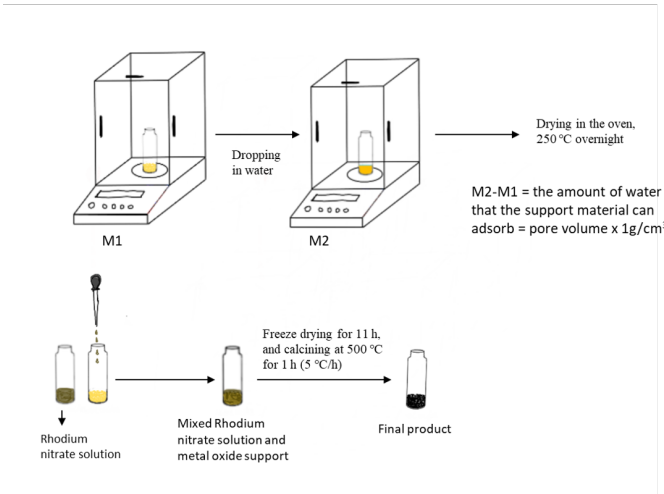

Figure 3.10: Impregnation process

3.3 Characterization of physicochemical properties

3.3.1 Nitrogen physisorption

Physisorption process

Physisorption is a phenomenon of non-specific intermolecular interaction between adsorbed molecules (adsorbate) and a solid material (adsorbent). It involves weak forces of molecular interaction (van der waals forces) and relatively low adsorption energy (usually in the range between 10-40 kJ/mol. Physical adsorption takes place on all surfaces provided that temperature and pressure conditions are favorable, and under proper conditions, it can result in adsorbed molecules forming multiple layers. Physisorption is thermodynamically reversible at isothermal conditions.
For nitrogen physisorption, when nitrogen gas is in contact with a solid at 77 K, a specific number of gas molecules will be attracted to the surface of the solid by van der Waals forces. The number of adsorbed N_2 molecules depends on the relative pressure of the N_2 gas in equilibrium with it. Relative pressure (p/p_0) is an dimensionless expression of the actual pressure p (at the temperature at which the experiment is performed) normalized to the saturation pressure p_0 (77 K, 101.3 kPa). The relationship between the number of molecules absorbed on the surface of solid and the relative pressure can be shown in one plot called adsorption isotherm, from which one can generate information about the specific surface area, pore structure, and size of the solid.

IPUAC physisorption isotherms

IUPAC Technical Report [97] summarizes six types of common physisorption isotherms (Figure 3.11) [98]. In summary, microporous structured materials generally correspond to Type I isotherms; non-porous or macroporous materials correspond to Type II isotherms; Type III and V isotherms show no identifiable multilayer formation, implying that adsorbent-adsorptive interactions are relatively weak; Type IV isotherms are usually given by mesoporous materials; and Type VI isotherms represent layer-by-layer adsorption on smooth, non-porous surfaces. Hysteresis loops are located in the multilayer range of physisorption isotherms and are generally associated with capillary condensation. This form of hysteresis can be attributed to adsorption metastability and/or network effects. There are five main types of the hysteresis loops. Type H1 loop exists in materials with a narrow range of uniform mesopores, and the steep, narrow loop is a clear sign of delayed condensation in the adsorption branch. Type H2 hysteresis loops are given by more complex mesoporous structures, with very steep desorption branches characteristic of the H2(a) loop, which can be attributed to pore blockage/penetration or cavitation in the pore neck in a narrow range of evaporation. H2(a) loop can be given by some ordered

mesoporous materials. H2(b) loop has also been associated with hole blockage, but the size distribution of the neck width is now much larger. The adsorption branch of the Type H3 is similar to the Type II isotherm, and the lower limit of the desorption branch is usually located at the cavitation-induced p/p_0. Loops of this type result from non-rigid aggregates of tabular particles, or macropores that are not fully filled with the pore condensate. The adsorption branch of H4 loop is a composite of Type I and Type II, and usually exists in mesoporous and micro-mesoporous materials. The H5 ring corresponds to some special structures. It contains open and partially blocked mesopores. The H3, H4, and H5 loops share the common feature of a sharp drop in the desorption branch within a narrow range of p/p_0 [97, 99].

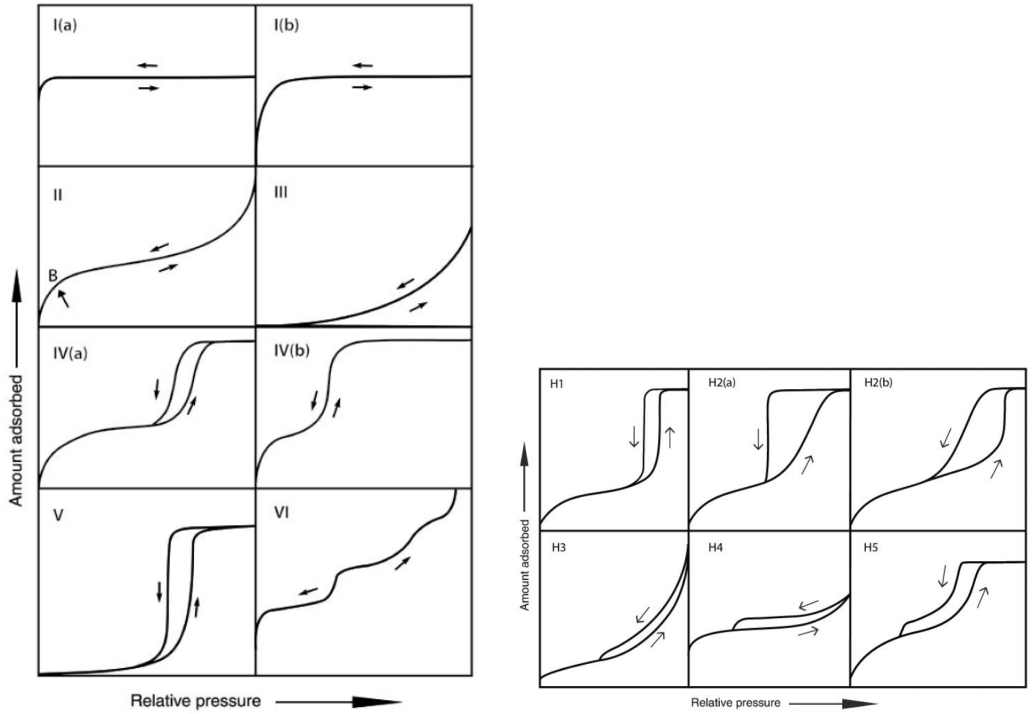

(a) Classification of physisorption isotherms. **(b)** Classification of hysteresis loops.

Figure 3.11: IUPAC physisorption isotherms [97].

Brunauer–Emmett–Teller (BET) model

The BET theory of adsorption generalized the Langmuir approach and included the treatment of multilayer adsorption. The theory assumes that: (a) The adsorbent's surface is uniform and the adsorption energy within the first layer is constant. (b) Except for the first layer, the adsorption energy of other layers is equal to the molar heat of condensation, and the condensation-evaporation conditions are exactly the same in these adsorption layers. (c) When p/p_0 approaches 1, the number of adsorption layers becomes infinite and the adsorbent condenses to a bulk liquid on the surface of the solid. Under dynamic equilibrium, the rate of adsorption on the

layer is equal to the desorption from the layer[100]. The BET equation was obtained by summing for an infinite number of adsorption layers :

$$\frac{1}{v[(\frac{p_0}{p})-1]} = \frac{(c-1)}{v_m c}(\frac{p}{p_0}) + \frac{1}{v_m c} \tag{3.1}$$

where v is the adsorbed gas quantity, v_m is the amount of gas adsorbed in the monolayer, p_0 is the saturation pressure of adsorbate, p is the equilibrium pressure of adsorbate, c is BET constant which equals to $exp(\frac{E_1-E_L}{RT})$, where E_1 is the heat of adsorption for the first layer, E_L is the heat of vaporization. From the equation a plot of $\frac{1}{v[(\frac{p_0}{p})-1]}$ vs $\frac{p}{p_0}$ yields a straight line in a range of $0.05 < \frac{p}{p_0} < 0.4$ with slope of $\frac{c-1}{v_m c}$ and intercept of $\frac{1}{v_m c}$, which can be used to calculate v_m and BET constant c. The BET surface area can then be calculated by the following equation 3.2:

$$S_{BET} = \frac{V_m L a}{V M} \tag{3.2}$$

where V_m is the monolayer adsorbed gas volume, L is Avogadro's number, which is $6.02 \cdot 10^{23}$ molecules/mol, a is the cross-sectional area of adsorbed gas molecules, V is the molar volume of adsorbed gas, M is the mass of the sample.

Measurement procedure

The specific surface areas (SSA) of the samples were characterized by nitrogen physisorption by a Micrometrics Tristar 3000 instrument using 150-350 mg of samples for the measurement. The samples were initially dried for at least 4 h at 250 °C under a nitrogen flow to remove water and other weakly adsorbed species. After the physisorption experiments were performed, the specific surface area was calculated by Brunauer–Emmett–Teller (BET) model. The porous structure of the samples is analyzed from the isothermal plots.

3.3.2 Chemisorption

Chemisorption process

In addition to physical adsorption, there is a chemical adsorption with stronger adsorption force, higher adsorption energy and higher requirements for adsorption conditions. Chemisorption involves the formation of chemical bonds between the adsorbate and the adsorbent which can be regarded as the formation of surface compounds. Due to the bond strength, chemical adsorption is difficult to reverse. Chemisorption occurs only between certain adsorptive and adsorbent species and only if the chemically active surface is cleaned of previously adsorbed molecules. Unlike physisorption, chemisorption usually forms single-layer adsorbed molecules

since it can only happen when the adsorptive can make direct contact with the surface.

Determination of metal area and average particles size

CO-chemisorption can be used to determine the metal dispersion, active surface area and active particle size with the monolayer assumption, which are important for the optimum design and efficient utilization of catalysts. The chemisorption isotherms can be performed by a secondary adsorption followed by desorption of physisorbed CO. The first adsorption includes both reversible physisorption and irreversible chemisorption, while the second adsorption is only the irreversible chemisorption.
The metal dispersion describes the ratio of the surface metal sites (the number of active metal atoms available for reaction) over total metal sites (the total number of metal atoms in the catalyst material):

$$D_{metal} = \frac{Q_{co} M_{metal} F_s}{W_{metal}} 100\% \tag{3.3}$$

where Q_{CO} is the quantity of chemisorbed CO monolayer per gram catalyst at STP (mol/g), M_{metal} is the molar mass of metal (g/mol), W_{metal} is the weight percentage of active metal over sample, and F_s is the stoichiometric factor, which refers the number of active metal atoms absorbed by one CO molecule.
The specific active metal area A_{metal} (cm^2/g) is determined by the area occupied by one surface molecule times the number of adsorbed molecules per gram:

$$A_{metal} = Q_{CO} F_s a_s N_A \tag{3.4}$$

a_s is the cross-sectional area of metal.
The particle (crystallite) size is further estimated by the specific active metal area and the weight percentage of active metal over sample, with the assumption that the crystallite shape is of regular geometry (here assume as hemispheres):

$$d_{metal} = \frac{6 \cdot W_{metal}}{A_{metal} \rho_{metal}} \tag{3.5}$$

ρ_{metal} is the density of the metal.

Measurement procedure

In order to remove the contaminants adsorbed on the surface and form the active sites, several pre-treatments were performed. In this project, the pretreatment involves the flow of O_2 followed by H_2 at 350 °C, and then flow in CO_2 at the same temperature. Each gas flowed for 30 min. After that, the adsorption isotherms were recorded using a Micromeritics ASAP 2020. The amount of sample used for each measurement was between 150 $\sim$ 200 mg.

3.3.3 Powder X-ray diffraction

X-ray scattering

X-rays can be considered as waves of electromagnetic radiation that can be imagined as a self-propagating transverse oscillating wave of electric and magnetic fields. Crystals are composed of a regular arrangement of atoms which consist a nucleus surrounded by a cloud of electrons. X-rays are scattered at the electrons of the atomic shell. During the scattering process the electron starts oscillating. It becomes a dipole and a spherical wave is sent out. When the wavelength and energy of the scattered wave does not change (elastic scattering), this process can also be called X-ray diffraction, the electron is known as the scatterer. A regular array of scatterers produces a regular array of spherical waves. In the majority of directions, these waves cancel each other out through destructive interference, however, they add constructively in a few specific directions, which can lead to the Bragg's law.

Bragg's law

The scheme of Bragg's law is shown in figure 3.12 [101].

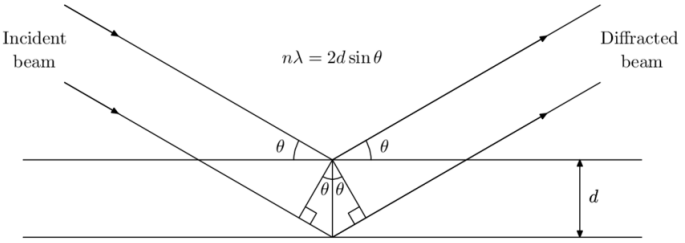

Figure 3.12: Scheme of Bragg's law [101].

This law states that when an X-ray is incident on a crystal surface, its angle of incidence θ is equal to the scattered angle of reflection, and when the interplanar spacing d is equal to the integer n of the wavelength, constructive interference will occur. Thus, Bragg's law can be expressed as:

$$n\lambda = 2dsin\theta \tag{3.6}$$

where λ is the wavelength of the X-ray.
The Bragg's law can be applied to calculate the lattice parameters. The lattice constant defines the size and shape of the unit cell of a crystal lattice, and the Lattice in three dimensions generally has six lattice constants: the lengths a, b, and c of the three cell edges, and the angles α, β, and γ between those edges (Fig. 3.13). For a specific kind of crystal, such as a simple cubic lattice, then $a = b = c$, α=β=γ=90 °C.

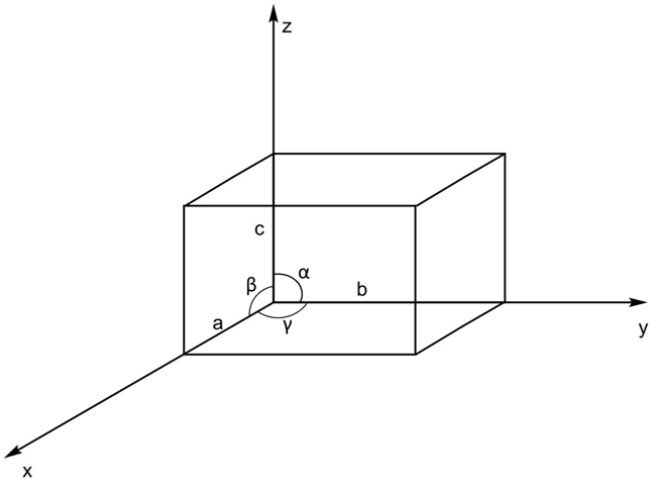

Figure 3.13: Lattice parameters

The interplanar spacing d_{hkl} is equal to the Miller indices (h, k, l which can be obtained from JCPDS card or COD card) and the lattice constant by this relation:

$$\frac{1}{{d_{hkl}}^2} = \frac{h^2}{a^2} + \frac{k^2}{b^2} + \frac{l^2}{c^2} \tag{3.7}$$

.
For a simple cubic lattice, since $a = b = c$, equation 3.7 can be derived as:

$$\frac{1}{{d_{hkl}}^2} = \frac{h^2 + k^2 + l^2}{a^2} \tag{3.8}$$

Then the lattice constant a can be calculated:

$$a = d_{hkl}\sqrt{h^2 + k^2 + l^2} \tag{3.9}$$

Scherrer equation
The average crystallite sizes were calculated from the widths of the corresponding XRD peaks using Scherrer Equation:

$$D = \frac{K\lambda}{\beta cos(\theta)} \tag{3.10}$$

Where, D = crystallites size (nm), $K = 0.89$ (Scherrer constant), $\lambda = 0.15406$ nm (wavelength of the X-ray source), β = FWHM (the peak brodening of half-maximum intensity at 2θ, radians), θ = Peak position (radians).
It is important to notice that the Scherrer equation assumes a perfect crystallinity without any other contribution to the peak width including instrumental broadening, which means the peak width would only be determined by the crystallite size.

Measurement procedure

The crystalline structures and solid solution purity of the samples were determined by Powder X-ray diffraction in a D8 Advance and D8 discover instrument with a

monochromatic CuKα radiation (1.54Å) in the 2θ range of 20 - 100 °. The scanning rate was 0.8 °/min. A transparent Si holder was used as the sample holder. To generate an X-ray source that is essentially monochromatic for the powder diffraction, a 0.02 mm Ni filter was used to remove the Kβ line that exists in the X-ray source. The results were collected by XRD wizard, and analysed in EVA and Igor 8.

3.3.4 X-ray Fluorescence Spectrometer

In an XRF measurement the sample is irradiated by X-rays, which induces an excitationprocess according to Figure 3.14 [102]. After the electrons in the inner layer of the elements in the sample are knocked out, the transition of the electrons outside the nucleus is caused. When the excited electrons return to the ground state, characteristic X-rays are emitted; Different elements emit their own characteristic X-rays, with different energy or wavelength characteristics. The detector accepts these X-rays, and the instrument software system converts them into corresponding signals, which are used for the composition analysis of materials.

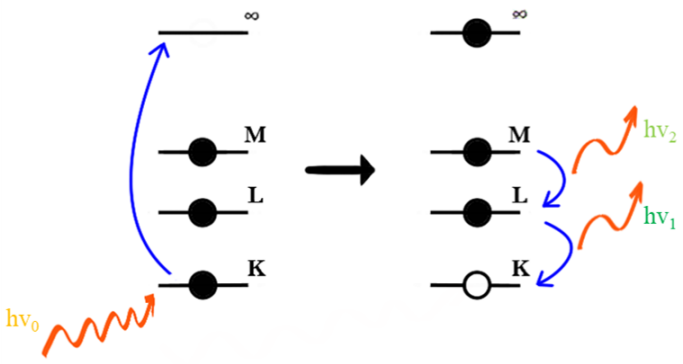

Figure 3.14: Schematic drawing of the X-ray fluorescence process [102].

3.4 Catalytic evaluation in a chemical flow reactor

Reactor set-up

A flow reactor was used for testing catalysts. The reactor is as shown in the figure below fig. 3.15, the interior is about 2 cm long. Quartz wool is placed where the two ends are connected to the gas tube to fix the sample and prevent the sample from being blown into the tube and Mass Spectrometry and cause contamination. There are graphite windows at the front and rear of the reactor to facilitate characterization of the catalyst and visualization of changes as the reaction proceeds. The catalyst was sieved to 40-80 μm in advance, each experiment used around 100 mg sample. After loading the sample, the reactor was mounted horizontally on a rack along the direction of the gas flow tube. There is a thermal couple put in the body of the reactor to regulate the reaction temperature. However, since the thermal couple is actually monitoring the temperature of the reactor body, the temperature of the catalyst during the reaction is unknown. In this regard, we tested the temperature collaboration in advance, and obtained a linear relationship, from which the actual temperature of the catalyst could be calculated according to the reactor temperature (fig. 3.16). The reactant gas flow is controlled by several Mass Flow Controllers (MFCs), and the total gas flow is balanced by Argon.
Gas flow composition was identified and quantified by Mass Spectrometry (MS). The interior of the MS is a high vacuum environment. The ion source is generated by electron ionization with an electron beam and separated according to their mass-to-charge ratio (m/z) in a magnetic field. The resolved ions will reach the detector and produce a m/z spectrum and the composition of the gas will be figured out. The conversion of feedstock can be calculated from equation (3.11) and the MS data:

$$X_{CO_2} = \frac{(CO_2)_{in} vol.\% - (CO_2)_{out} vol.\%}{(CO_2)_{in} vol.\%} \tag{3.11}$$

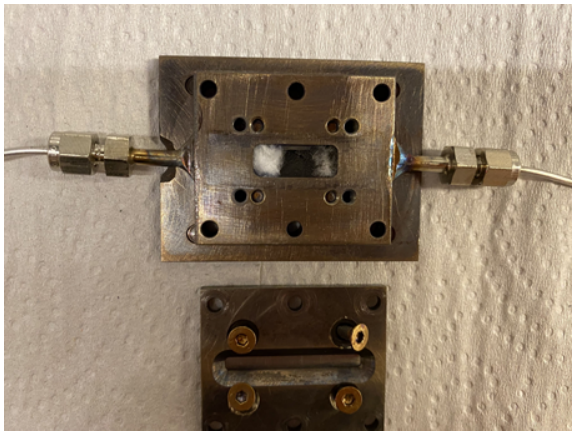

Figure 3.15: Flow reactor

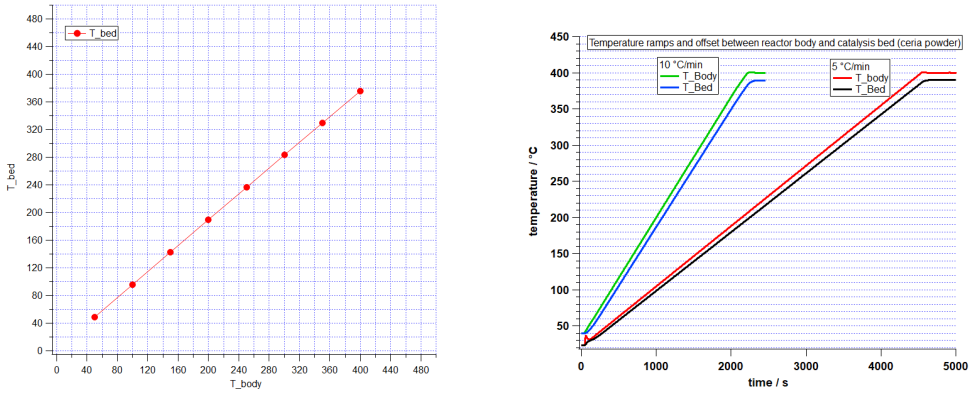

(a) Temperature calibration between reactor body and catalysis bed

(b) Temperature ramps and offset between reactor body and catalysis bed

Figure 3.16: Temp and ramps between reactor body and catalysis bed

Measurement procedure

The reactor was used to test the performance of C80SO, C80FO supported Rh catalysts and Rh doped cerium oxides in CO_2 methanation reaction. At beginning, the balance gas Ar was used to purge away the air contained in the reactor. Followed by heating up to 40 °C to get a stable start point before heating up to the first experiment temperature 150 °C. After the temperature reached 150 °C, start to flow in the 99 vol.% CO_2 (0.8 ml/min). The other experiment temperatures are 250, 350 and 400 °C. At each temperature points, three 20 min H_2 pulses were set to better observe the performance of the catalyst. When the reaction at each temperature points was completed, the temperature was lowered to room temperature in the flow of CO_2, and then all flows were turned off. The total flow for the experiment was kept constant at 150 ml/min.

4

Results and discussion

4.1 Properties of doped ceria materials

4.1.1 Specific surface area and porosity

The SSA was measured with N_2-physisorption using the BET method, and the porosity of the materials was analysed from isothermal plots. Table 4.1 shows the SSAs of the samples sorted by different methods. The detailed information about the samples are shown in Appendix table A.1.

Influence of synthesis methods

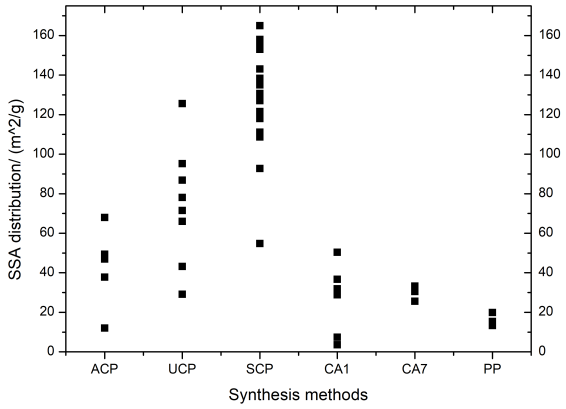

Figure 4.1: SSA distribution of different methods

From the results, it is clear that the SSAs of the samples prepared by the co-precipitation methods are generally higher than that of the samples prepared by gel and polymeric precursor methods. Especially SSAs of the samples synthesised by sodium hydroxide method, are larger than that of the samples synthesized by other methods with the same dopant and composition, up to 167 m^2/g (sample 32 C99RO-SCP-F350). The samples synthesized by urea method also generated good SSAs, especially the samples calcined at 350 ° C, the SSAs can exceed 100 m^2/g for CeO_2. The ammonia method, however, cannot perform as well as the other two

Table 4.1: Specific surface areas of the samples

Method	Sample Name	S_{BET} (m^2/g)	NO.
Ammonia method	C80SO-ACP-F500	37.8	1
	C80FO-ACP-F500	46.9	5
	CeO2-ACP-F500	49.4	6
	C80SO-ACP-F350	68	25
	C80SO-ACP-F500	12	25
Urea method	C80SO-UCP-F350	86.8	12
	C80SO-UCP-F500	43.17	12
	C80SO-UCP-F350	71.5	19
	C80SO-UCP-F500	29.1	19
	CeO2-UCP-F350	125.6	14
	CeO2-UCP-F500	78.1	14
	C80FO-UCP-F350	95.2	15
	C80FO-UCP-F500	66	15
Sodium hydroxide method	C80SO-SCP-F350	135	16
	C80SO-SCP-F500	108.7	16
	C80SO-SCP-F500	118	36
	C60SO-SCP-F350	136	28
	C60SO-SCP-F500	108.8	37
	C50SO-SCP-F350	127	26
	C80FO-SCP-F350	118.9	17
	C80FO-SCP-F500	92.7	17
	C80FO-SCP-F500	153	38
	C60FO-SCP-F350	137	29
	C50FO-SCP-F350	136	27
	C50FO-SCP-F500	54.8	27
	C985PO-SCP-F350	143.1	20
	C985PO-SCP-F500	130.7	20
	C97PO-SCP-F350	158	30
	C91RO-SCP-F350	120.6	31
	C91RO-SCP-F500	111.1	31
	C95RO-SCP-F350	156.9	21
	C95RO-SCP-F500	138.4	21
	C99RO-SCP-F350	154.8	32
	C99RO-SCP-F500	136.3	32
	CeO2-SCP-F350	165	22
	CeO2-SCP-F500	121.5	22
Citric acid method	C80SO-CA1-F500	7.41	2
	C80SO-CA7-F500	25.6	3
	C80SO-CA7-F500	33.3	4
	CeO2-CA1-F150,500	3.57	9
	CeO2-CA7-F500	25.6	7
	C80FO-CA1-F500	36.7	11
	C80FO-CA7-F500	30.5	18
	C50FO-CA1-F500	31.9	34
	C97PO-CA1-F500	28.8	23
	C95RO-CA1-F500	50.4	24
Modified Pechini method	C80SO-PP-F500	15.4	8
	CeO2-PP-F500	19.9	10
	C80FO-PP-F500	13.3	13
	C50FO-PP-F500	13.3	35

ACP - Co-precipitation with ammonia (Ammonia method);
UCP - Co-precipitation with urea (Urea method);
SCP - Co-precipitation with sodium hydroxide (Sodium hydroxide method);
CA1- Citric acid method ($pH \approx 1$);
CA7- Citric acid method ($pH \approx 7$);
PP- Modified Pechini method;
F150 - calcination temperature = 150 °C;
F350 - calcination temperature = 350 °C;
F500 - calcination temperature = 500 °C;

co-precipitation methods in generating high SSAs. The highest is 49.4 m^2/g for ceria sample.

The diversity of the SSAs of the three methods may be due to the different precipitants and synthesis steps. Both urea and sodium hydroxide methods have a heating step in the synthesis process. The SSAs of the corresponding products are higher than the samples synthesised by ammonia method without a heating step. It thus seems that the temperature has an effect on the SSA. In order to verify this conjecture, sample 25 (C80SO-ACP-F350, C80SO-ACP-F500) was synthesized by applying the sodium hydroxide method but substituted precipitant, is ammonia. The results are 68 m^2/g (350 °C) and 12 m^2/g (500 °C). Comparing the sample calcined at 500 °C with the same composition synthesized by ammonia method without the heating step (1 C80SO-ACP-F500, 37.8 m^2/g), the SSA turns out to be smaller, which supports that the high temperature during synthesis procedure seems helpless in generating high SSA. By comparing the SSAs of sample 16 with sample 25, it can be seen that the precipitant plays a role in high SSAs formation, NaOH is better than NH_4OH in this respect.

Compared with other methods, the SSAs of the samples obtained by citric acid method are quite unstable, and different pH, drying conditions, calcination conditions, etc. have a great influence on the results (more on this later). Among them, the results of the citric acid method samples obtained in a neutral environment and dried on a heating plate at 201 °C for five hours are relatively higher. The SSAs of the samples obtained by modified Pechini method are stable between 10 and 20 m^2/g. It's consistent with the conclusions obtained in other articles that Pechini method is suitable to obtain solid solutions but can't generate high surface areas [98].

Influence of calcination temperature

Some samples synthesized by the urea method and the sodium hydroxide method were calcined at different temperatures. From the results, it can be seen that the calcination temperature has a significant effect on the surface areas of the samples. The higher the calcination temperature, the lower the surface area. Especially for the urea method, the sample's surface area obtained at 500 °C is nearly half than that of 350 °C. The samarium-doped samples (C80SO) No. 12 and 19 were both synthesised by urea method, but generate different results. This may be due to the different reflux temperature and time of the two samples during the synthesis process, as well as the different aging time (For sample No.12 it was refluxed at 100 °C for 15 h, aged for around 1 hour, after that was brought to be boiled for a while. While for sample No.19, it was refluxed at 91 °C for 8 h and then aged overnight.).

Sample 25 synthesized by the sodium hydroxide method but using ammonia as the precipitant also showes a great drop in SSA when the calcination temperature was increased, and the decrease was more obvious (68 m^2/g to 12 m^2/g) than that of urea method. Overall, the sodium hydroxide method samples were more stable compared with other methods' samples, and increasing the calcination temperature had the

least effect on the SSAs.

Drying method and pH for citric acid method samples

At the beginning, the pH environment was considered as a factor that influences the SSAs of citric acid method samples. For the Sm-doped cerium samples synthesized by citric acid method, a neutral environment ($pH \approx 7$) seems more beneficial to obtain a higher surface area than an acidic environment ($pH \approx 1$), it can be seen by comparing sample No. 2, 3 and 4. This may be because after increasing the pH of the solution, more carboxylic acid groups in the citric acid are deprotonated, and the sites that can bind to metal cations are more and stronger, and sintering is not easy to occur after high temperature calcination. The surface area of the product is also relatively high. A similar result was observed by the CeO_2 samples synthesized in different pH environments (samples No. 7 and 9, with surface areas of 36.7 and 3.57 m^2/g respectively). However, it should be noted that sample No. 9 was calcined at two conditions (150 °C for 9 h and 500 °C for 5 h) without pyrolysis process, which might be the other cause for the low surface area of the sample. For Fe-doped ceria, it seems that the sample obtained in an acidic environment has a higher SSA. Nonetheless, the accuracy of this result needs to be verified, because during the evaporation process of synthesizing, some yellow fine precipitates appeared in the solution, which could be $Fe(OH)_3$ ($Ksp = 10^{-37}$, can precipitate in acidic environment), and the high specific surface area may be due to the appearance of the fine particles.

The drying process in citric acid method can also be noticed as an influencing factor for SSAs when comparing the results of samples No.3 and 4. It seems that drying on the heating plate at 201 °C is beneficial for generating higher surface areas compared with drying in the oven. This may be because after adjusting the solution pH with ammonia, the ammonium ions and the nitrate ions from the metal precursors combine together to form ammonium nitrate. During the drying process in the oven, the ammonium nitrate decomposes to form water and nitrous oxide, citric acid can also decompose to water and CO_2, the decomposition affects the temperature inside the sample (especially the decomposition of ammonia that releases a lot of heat), which influences the structure of the sample and reduces its SSA. While drying on the heating plate, with the help of a temperature meter, it's easier to regulate and stabilize the sample's temperature.

The samples synthesized later (No. 23, 24, 34) also verify that a stable drying temperature is more beneficial to obtain samples with higher SSAs. Although these samples were all generated in an acidic environment with $pH \approx 1$, they were all dried on a heating plate, and the surface area could even reach 50.4 m^2/g. A potential contributor to the change of temperature inside sample at pH=1 may be the decomposition of citric acid or cerium citrate. Citric acid can decompose into water and carbon dioxide at 175 °C, while cerium citrate has an exothermic decomposition process between 195 °C and 310 °C that decomposes into violent residuals and cerium carbonate [103]. Nevertheless, since the samples synthesized later did not have the same composition as the samples synthesized under the condition of

$pH \approx 7$ as a control, it may not be rigorous to simply say that a stable drying temperature is more beneficial to obtain a higher SSA. Perhaps the sample components as well as different dopants also contributed.

Sample composition

The influence of sample composition on SSAs was also investigated using sodium hydroxide methods. For Sm doped sample, with the increase of Sm content from 0.2 to 0.6 (molar ratio), the surface area didn't change too much. When the content of Sm reached 0.5, the surface area dropped a bit. This might be the formation of Sm_2O_3 (more in XRD part). Two batches of C80FO-SCP-F500 samples (No. 17 and 38) showed a big difference in surface areas. The only difference is that sample 38 was directly calcined at 500 °C for 5 h with the heating rate of 4 °C/min, sample 17 was first calcined at 350 °C and then calcined at 500 °C for 5 h with the same heating rate. This may be due to the effect of the secondary calcination on the already formed crystal structure, and sintering may occur, resulting in a reduction in the specific surface area. The same thing also happened to the Sm-doped samples with the same condition (sample 16 and 36).

4.1.2 Sample structures

Based on the isothermal data generated from N_2-physisorption, the structures can be estimated, and based on the Brunauer–Emmett–Teller (BET) method the so-called BET surface areas can be calculated The analysis of the porous structures was mainly based on the IUPAC Technical Report [97], chapter 4. The referenced types physisorption isotherms and hysteresis loops can be checked in fig. 3.11. In this part, to better compare the isotherms of different samples, some of them were plotted together in one figure. The detailed isotherms for each sample can be checked in Appendix A.2

Ammonia method isotherms

From fig. 4.2, for the Sm-doped ceria sample, at the low p/p_0 region, the amount of adsorption increases slowly, which indicates that N_2 molecules are adsorbed on the inner surface of the mesoporous in a single layer to multiple layers. A hysteresis loop shows up at medium pressure region without a saturated adsorption platform, showing that the pore structure is very irregular. The desorption branch of the loop is very steep at $p/p_0 = 0.4$ - 0.6, which can be attributed to the pore blockage/permeation or evaporation caused by cavitation in the narrow range of pore necks. The shape of the hysteresis loop is similar to the shape of H5 type loop according to IUPAC [97], which has a distinctive form associated with certain pore structures containing both open and partially blocked mesopores. For pure ceria and Fe-doped ceria, the isotherms are concave without inflection point, therefore no identifiable monolayer forms and the adsorbent-adsorbate interactions are relatively weak, and

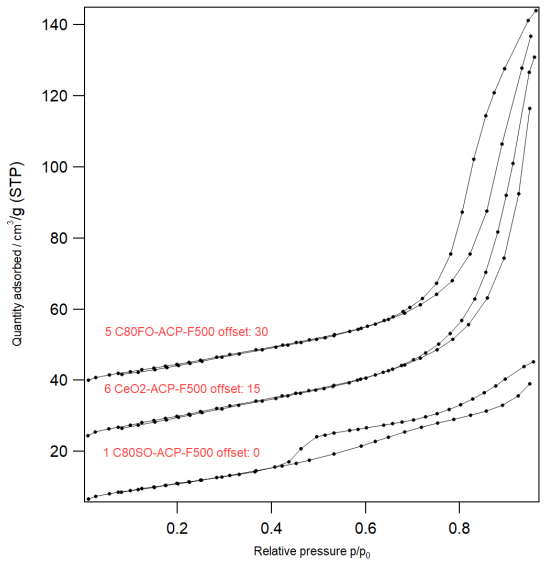

Figure 4.2: Isotherms for ammonia method samples

the adsorbed molecules are clustered around the most favorable sites on the surface of a nonporous or macroporous solid. The narrow and steep hysteresis loops at the high relative pressure region might be caused by delayed condensations on the adsorption branch, and the finite adsorption at the saturated pressure showed the irregular porous structures.

Urea method isotherms

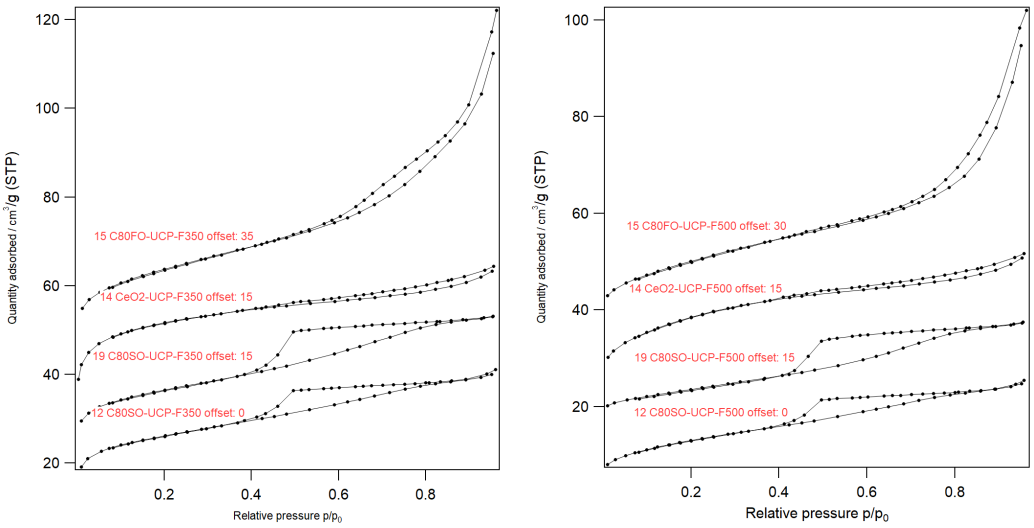

Figure 4.3: Isotherms for urea method samples (left: calcined at 350 °C; right: calcined at 500 °C)

For urea method products, the isotherm shapes of different dopants are very differ-

ent, which proves that different dopants have different impact on the pore structure of cerium oxide. At the same time, different calcination temperatures have little effect on the isotherm trend for samples with the same composition. The urea method samples exhibit significant steep adsorption at very low P/P_0. This may be due to the presence of micropores, and the enhanced adsorbent-adsorption interaction in the micropores leads to the filling of micropores at very low P/P_0. It is worth noting that for the samples with the same composition, the micropore filling phenomenon of the product calcined at 350 °C is more significant than that of the product calcined at 500 °C.

The samples doped with Sm have wide hysteresis loop, and the desorption branches are very steep, which are similar to the shape of the H2 hysteresis loop in IUPAC [97]. Those characters suggest that the pore structure of the samples are more complicated and the phenomenon of pore blocking was occur. The upward trend of the isotherm in the high P/P_0 zone proves that the particle accumulations are not uniform in the samples. Fe-doped samples have very narrow and sharp hysteresis loops without adsorption saturation, which is similar to Type H3 hysteresis loop that are given by non-rigid aggregates of plate-like particles but also if the pore network consists of macropores which are not completely filled with pore condensate. Further, at low P/P_0 region, the adsorbent-adsorption interaction in the micropores of Fe-doped samples are not as significant as other composition samples. For pure ceria samples, the characteristics of isotherms obtained by physisorption on mesoporous and micro-mesoporous adsorbents (Type H4) can be clearly seen. This shape is the result of unrestricted monolayer-multilayer adsorption up to high p/p_0.

Sodium hydroxide method isotherms

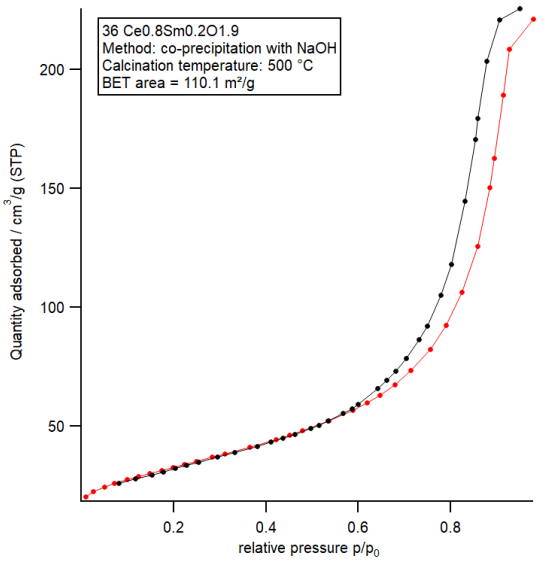

Figure 4.4: Isotherm for sample $Ce_{0.8}Sm_{0.2}O_{1.9}$ synthesised with sodium hydroxide method

Unlike the samples made by urea method, the isothermal plots for the samples made by the sodium hydroxide method samples showed fewer differences between the different dopants and different calcination temperatures (detail pics in Appendix A.2.3). Here one typical isotherm of a sodium hydroxide method sample is shown (fig. 4.4). It can be seen that the isotherm has a steep and narrow loop, which is a clear sign of pore condensation in the mesoporous structure, and the adsorption platform at P/P_0 zone reflects a uniform pore size distribution. The similar isotherms show that the pore structures of the samples obtained by the sodium hydroxide method are similar. This method is also a relatively stable synthesis method, different dopants and calcination temperatures have little effect on the structures of the samples obtained by this method.

Citric acid method isotherms

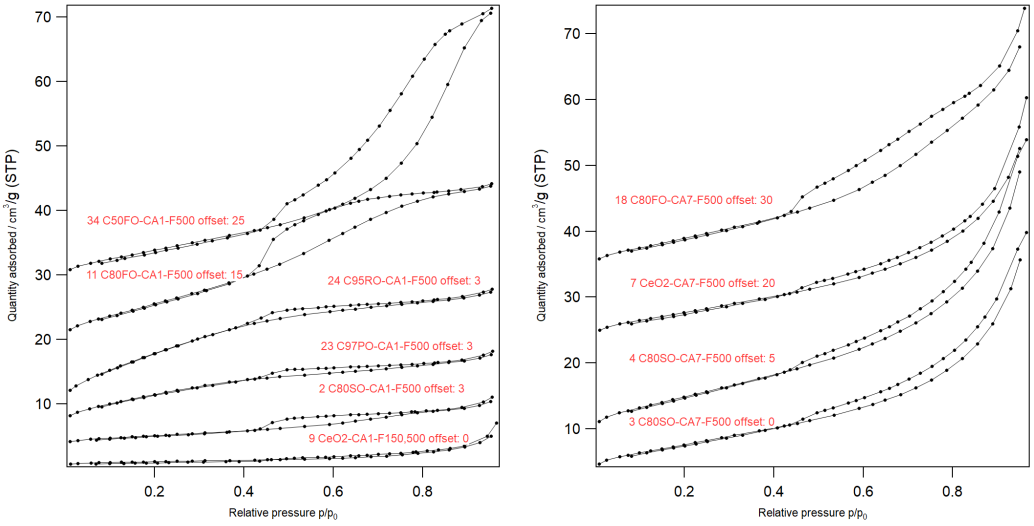

Figure 4.5: Isotherms for citric acid method samples (left: pH=1; right: pH=7)

It can be seen from Fig. 4.5 that the structures of the citric acid method samples synthesised at different pH are quite different. For Sm, Pt and Rh doped samples synthesised at $pH \approx 1$, the hysteresis loop indicates a complicated pore structure and mesoporous and micro-mesoporous. The rising trend of the isotherm at high P/P_0 may be due to the occurrence of further multilayer adsorption. The pure ceria synthesised at $pH \approx 1$ is kind of special since it was calcined at 2 different temperatures(1 °C/min to 150 °C, keep for 9h, and 4 °C/min to 500 °C for 5h). At P/P_0= 0 - 0.45, the amount of absorption is higher than desportion, which may be due to an operating error that the sample measured in N_2-physisorption is not dried enough. The general shape of the pure ceria isotherm showed an insignificant adsorbent-adsorption interaction, and the adsorbed molecules may cluster around the most favorable sites on the surface of a nonporous or macroporous solid. The steep increase at P/P_0=1 shows an increased thickness of adsorbed multilayers without limit.

The isotherm of 34 C50FO-CA1-F500 synthesised at $pH \approx 1$ is more like the type H5 hysteresis loop, which indicates that the material has open and partially blocked mesoporous structure, while the other Fe-doped ceria (11 C80FO-CA1-F500 sample)

shows a typical H2 type hysteresis loop with the funnel shape, that represented pore blockage/penetration or cavitation in the pore neck.
The isotherms of the samples synthesised at $pH \approx 7$ looks quite similar. The adsorbent-adsorbate interactions are relatively weak and the amount adsorbed seems infinite at the saturation pressure. The hysteresis loops are similar to type H3 loop, which usually exists in materials with non-rigid aggregates of tabular particles, or macropores. For Fe doped sample synthesised at $pH \approx 7$, the hysteresis loop is more obvious, which might be attributed to adsorption metastability and/or network effects.

Modified Pechini method isotherms

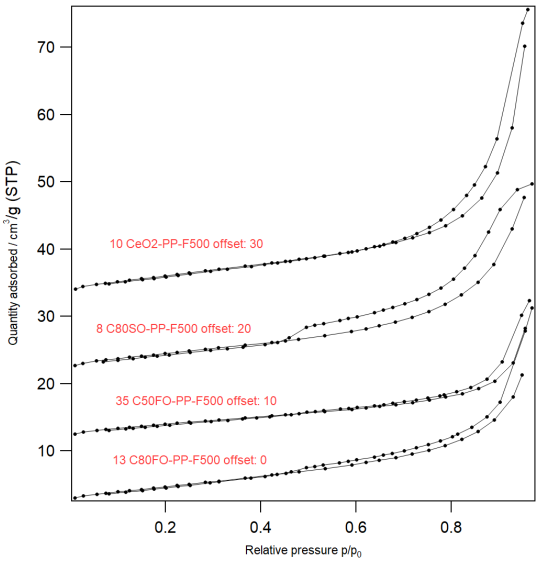

Figure 4.6: Isotherms for modified Pechini method samples

The pechini method samples seem to have weak interaction with N_2. For 8 C80SO-PP-F500 and 13 C80FO-PP-F500 isotherms, they are quite similar to type H5 hysteresis loop, which is associated with certain pore structures containing both open and partially blocked mesopores. For pure ceria and 35 C50FO-PP-F500, the steep and narrow hysteresis loops look like the H1 type, which represents the existence of a uniform mesoporous structure in a narrow range.

4.1.3 Crystallinity and crystallite size

The diffraction patterns of the as-prepared samples were recorded over a 2θ range of 20 ° to 100 °. The observed diffraction peaks are assigned to the crystalline cubic structure of the CeO_2 phase (COD card No. 9009008), except the Fe-doped sample synthesised by urea method and calcined at 500 °C, which has some extra peaks that could be assigned to the crystalline trigonal structure of α-Fe_2O_3 phase (COD card No. 9009782).

According to the XRD results, the lattice constant of the samples was calculated based on the Bragg's law and referenced the Miller indices of a CeO_2 with cubic structure (COD card No. 9009008) as standard. Since the crystal lattice of the samples is assigned to simple cubic, all the sides are equal so the lattice constants have a relation of $a = b = c$, the lattice constant then can be calculated by the equation: $a = d_{hkl} \cdot \sqrt{(h^2 + k^2 + l^2)}$. The crystallite sizes were calculated by Scherrer equation. The final results were shown in table 4.2.

Ammonia method samples

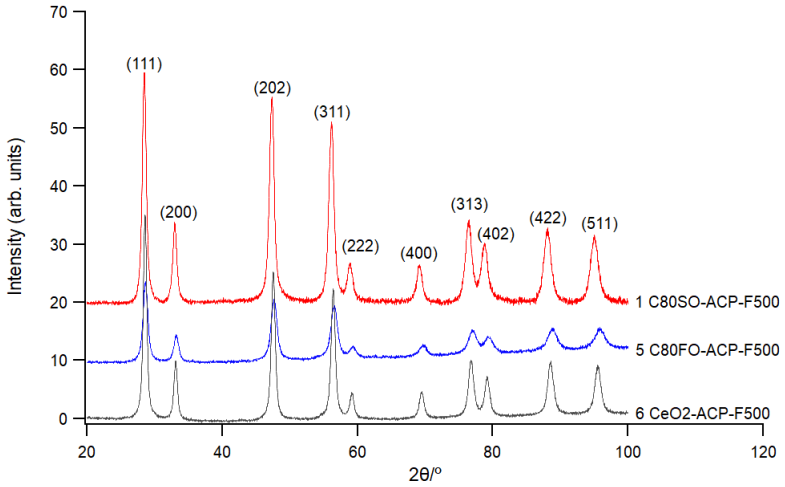

Figure 4.7: Diffraction pattern of ammonia method samples

The diffraction pattern of ammonia method samples (fig. 4.7)showed no impurity peaks that related to iron oxide or samarium oxide for Fe and Sm doped ceria samples compared with the pure ceria sample, indicating that the as-prepared mixed oxides were crystallized in a single phase. It can also be seen from the figure that the characteristic peaks of Fe-doped sample shifted to the higher 2θ angle compared to pure cerium oxide, while the characteristic peaks of Sm-doped sample shifted to the higher 2θ angle, showing the lattice parameter of cerium oxide had changed, which further showed that the Fe ions and Sm ions were doped into the crystal lattice of cerium oxide, and pure solid mixtures were obtained. This conclusion can also be supported by the calculated lattice constant (Table 4.2). The ion radii of Fe^{3+} (0.64 Å) is smaller than that of Ce^{4+} (0.97 Å), and the obtained sample lattice constant is also smaller than that of pure cerium oxide. The opposite is true for Sm^{3+}. The diffraction peak of Fe-doped sample is broader than others, that showed the crystallite size is smaller than pure ceria and Sm-doped sample, which is in line

Table 4.2: Lattice constant and crystalline size of the samples

Method	Sample Name	S_{BET} (m^2/g)	Lattice Constant (a)(Å)	D_{XRD} (nm)	NO.
Ammonia method	C80SO-ACP-F500	37.8	5.43002	9.38	1
	CeO2-ACP-F500	49.4	5.40786	11.49	6
	C80FO-ACP-F500	46.9	5.39384	8.05	5
Urea method	C80SO-UCP-F350	86.8	5.43625	5.28	12
	C80SO-UCP-F500	43.17	5.43533	7.56	12
	C80SO-UCP-F350	71.5	5.43040	6.19	19
	C80SO-UCP-F500	29.1	5.42958	9.67	19
	CeO2-UCP-F350	125.6	5.41478	6.02	14
	CeO2-UCP-F500	78.1	5.41116	8.26	14
	C80FO-UCP-F350	95.2	5.41149	6.33	15
	C80FO-UCP-F500	66	5.39789	5.69	15
Sodium hydroxide method	C80SO-SCP-F350	135	5.42702	4.85	16
	C80SO-SCP-F500	108.7	5.42455	5.31	16
	C80SO-SCP-F500	118	5.41992	5.25	36
	C60SO-SCP-F350	136	5.44278	4.86	28
	C60SO-SCP-F500	108.8	5.44269	5.34	37
	C50SO-SCP-F350	127	5.44814	5.03	26
	CeO2-SCP-F350	165	5.39486	4.32	22
	CeO2-SCP-F500	121.5	5.40432	5.10	22
	C80FO-SCP-F350	118.9	5.37103	4.72	17
	C80FO-SCP-F500	92.7	5.37132	4.94	17
	C80FO-SCP-F500	153	5.39221	4.32	38
	C60FO-SCP-F350	137	5.97	3.72	29
	C50FO-SCP-F350	136	6.75457	5.01	27
	C985PO-SCP-F350	143.1	5.40425	4.75	20
	C985PO-SCP-F500	130.7	5.40875	5.04	20
	C97PO-SCP-F350	158	5.40499	4.64	30
	C99RO-SCP-F350	154.8	5.40107	4.41	32
	C95RO-SCP-F350	156.9	5.39999	4.31	21
	C95RO-SCP-F500	138.4	5.39876	4.64	21
	C91RO-SCP-F350	120.6	5.39751	5.01	31
Citric acid method	C80SO-CA1-F500	7.41	5.43554	10.95	2
	CeO2-CA1-F150,500	3.57	5.41074	24.54	9
	C80FO-CA1-F500	36.7	5.38681	4.97	11
	C50FO-CA1-F500	31.9	5.92061	4.51	34
	C97PO-CA1-F500	28.8	5.41170	7.66	23
	C95RO-CA1-F500	50.4	5.40645	5.81	24
	C80SO-CA7-F500	25.6	5.43965	11.57	3
	C80SO-CA7-F500	33.3	5.43341	11.01	4
	CeO2-CA7-F500	25.6	5.4082	14.37	7
	C80FO-CA7-F500	30.5	5.39171	6.37	18
Modified Pechini method	C80SO-PP-F500	15.4	5.42971	12.97	8
	CeO2-PP-F50	19.9	5.40933	16.49	10
	C80FO-PP-F500	13.3	5.38843	4.33	13
	C50FO-PP-F500	13.3	5.34103	4.26	35

ACP - Co-precipitation with ammonia (Ammonia method);
UCP - Co-precipitation with urea (Urea method);
SCP - Co-precipitation with sodium hydroxide (Sodium hydroxide method);
CA1- Citric acid method ($pH \approx 1$);
CA7- Citric acid method ($pH \approx 7$);
PP- Modified Pechini method;
F150 - calcination temperature = 150 °C;
F350 - calcination temperature = 350 °C;
F500 - calcination temperature = 500 °C;

with the calculated crystallite size results.

Urea method samples

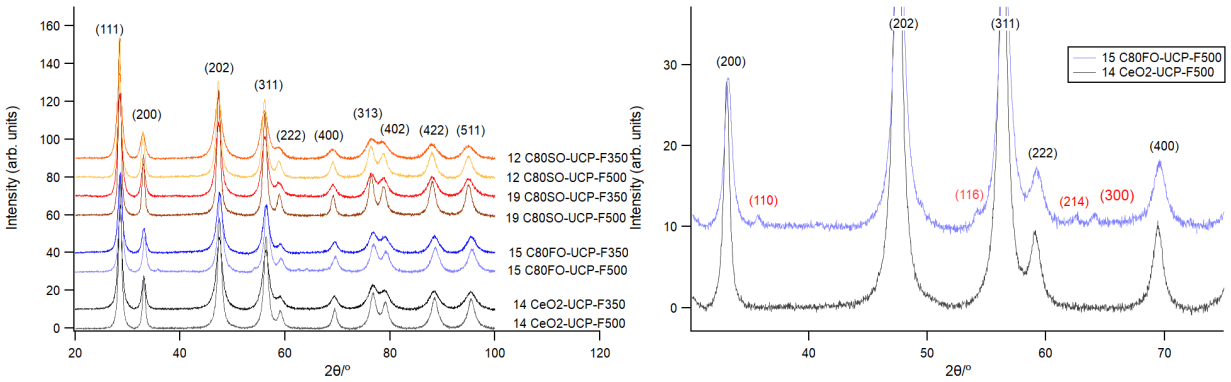

Figure 4.8: Left: diffraction pattern of urea method samples; right: detail pattern of C80FO-UCP-F500

Figure 4.8 shows the XRD pattern of the samples synthesized by urea method. It can be clearly seen that in addition to the introduction of different metal ions, the calcination temperatures also affect the shifts of the characteristic peaks. For all oxides of the same composition, the characteristic peaks appear to shift to the lower 2θ angle at relatively high calcination temperatures, showing the lattice parameter increase, which is in line with the calculated lattice constant. Moreover, the peaks of the samples obtained at 500 °C are sharper and higher in intensity than that of the sample at 350 °C, which means the crystallinity and crystal size of the samples are higher. It can be seen from table 4.2, with the increase of calcination temperature, the crystallite sizes decreased for Sm-doped ceria and cerium oxide. The reason why the crystallite size decreased might be the appearance of Fe_2O_3. Some impurity peaks appeared in the XRD pattern of sample C80FO-UCP-F500, and those peaks

are assigned to α-Fe_2O_3.

Sodium hydroxide method samples

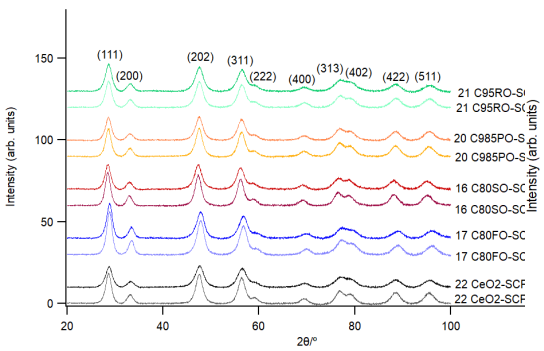

(a) Diffraction pattern of sodium hydroxide method samples with different dopants

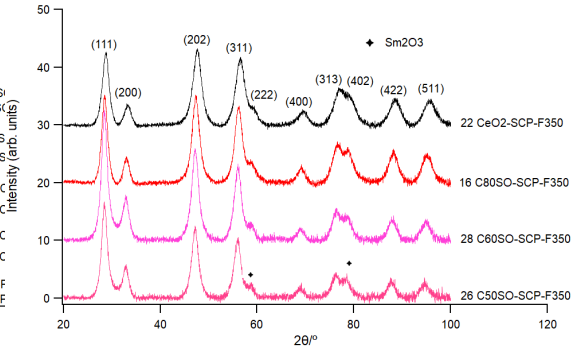

(b) Diffraction pattern of Sm-doped sodium hydroxide method samples with different compositions

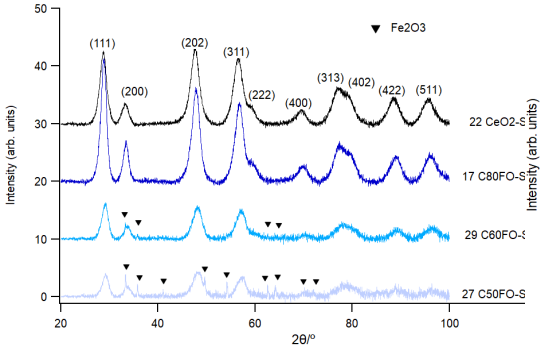

(c) Diffraction pattern of Fe-doped sodium hydroxide method samples with different compositions

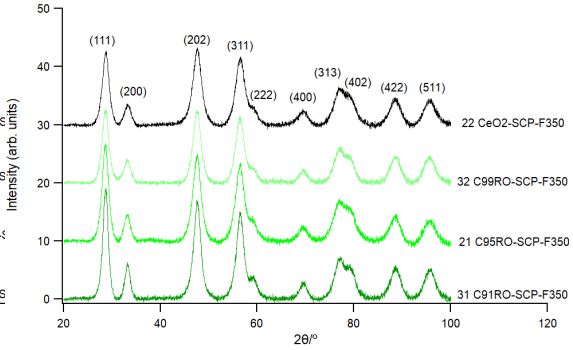

(d) Diffraction pattern of Rh-doped sodium hydroxide method samples with different compositions

Figure 4.9: Diffraction pattern of ammonia method samples

The XRD peak of the sodium hydroxide method sample also exhibited shifts relative to the pure cerium oxide in the Sm and Fe-doped ceria samples, but the characteristic peak shifts of the samples with Pt and Rh dopants are not so obvious (Fig. 4.9a). Since there are no impurity peaks, this may be due to the low content of Pt and Rh in the samples. Compared with other methods, the XRD peaks of the JM method samples are generally wider and have a lower peak intensity, which proves that the obtained sample may have a smaller crystallite size, but there is an obvious phenomenon that the characteristic peaks become narrower and stronger in intensity due to the increase in the calcination temperature, which proves once again the particle growth due to the calcination temperature.
Figure 4.9b, 4.9c and 4.9d compared the Sm, Fe and Rh doped ceria with different dopant compositions. The Sm_2O_3 phase started to show up when the molar percentage of Sm reached 50 %, while for Fe-doped sample the solubility of iron was 40

% in this case. There is an obvious peak shift to the lower 2θ angle with the increase of Sm molar percentage in ceria, even for the C50SO-SCP-F350 sample. It might be because of the low content of Rh that Rh-doped sample didn't show significant peak shift or impurity peaks, but the shape of peaks became narrower and more intense with the increase of Rh molar percentage. At the same time, the lattice constant decreased, this is in line with the ionic radii of Rh and Ce ions (0.67Å and 0.97Å respectively). The crystallite size increased, this also influenced the SSAs of the Rh-doped samples that dropped with the increase of Rh content (see in table 4.2).

Citric acid and modified Pechini method samples

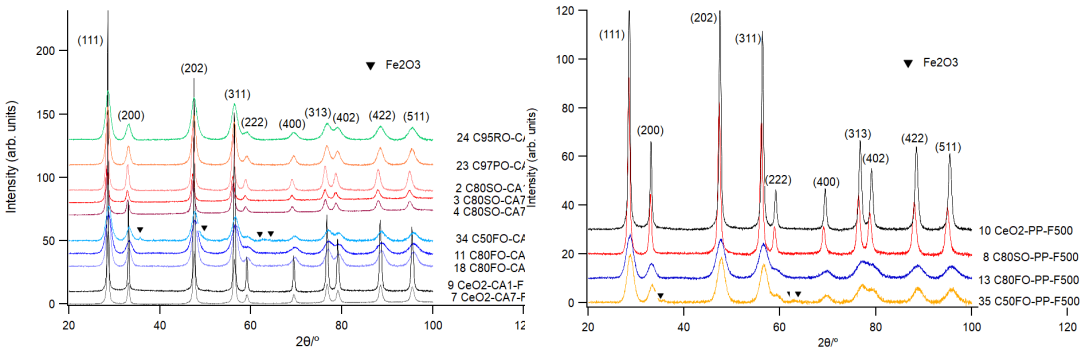

(a) Diffraction pattern of citric acid method samples

(b) Diffraction pattern of modified Pechini method samples

Figure 4.10: Diffraction pattern of ammonia method samples

The XRD characteristic peaks of the samples synthesized by citric acid method (Fig. 4.10a) also show peak shifts at the 2θ axis after the introduction of different dopants, which proved that the metal ions successfully doped into the crystal lattice of ceria and caused the change of the lattice parameter. Similar to the sodium hydroxide method, the peak shifts of the samples doped with Pt and Rh are also not obvious because of the low doped ion content. Compared with other methods, the peak intensities of the samples synthesized by this method and modified Pechini method are higher, while the SSAs of the corresponding samples are lower.

Comparison of CeO_2 and $Ce_{0.5}Fe_{0.5}O_{1.75}$ samples synthesised by different

methods

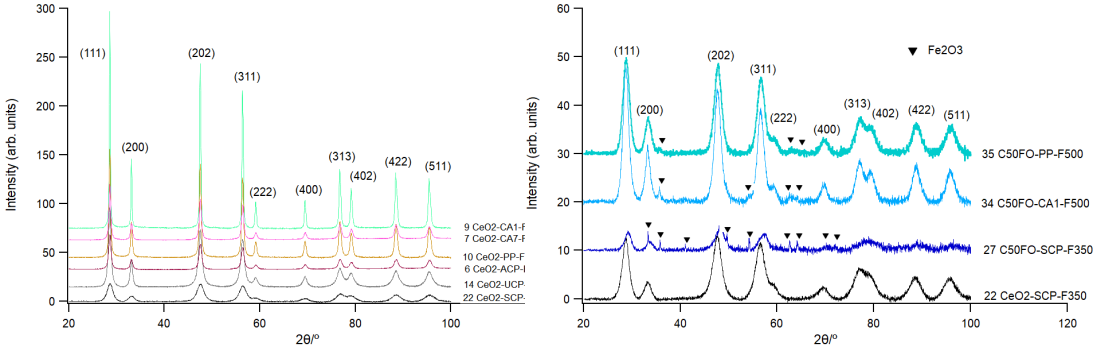

(a) Diffraction pattern of CeO_2 samples synthesised by different methods

(b) Diffraction pattern of CeO_2 samples synthesised by SCP, CA and PP methods

Figure 4.11: Comparison of CeO_2 and $Ce_{0.5}Fe_{0.5}O_{1.75}$ samples synthesised by different methods

Fig. 4.11a compares the XRD patterns of pure cerium oxide obtained by different methods at 500 °C. It can be found that the cerium oxides synthesized by any method are pure, and there are no impurity peaks or peak shifts at the 2θ axis that should not appear. The samples obtained by the citric acid and modified Pechini methods have significantly larger crystallites as one would expect after higher temperature treatment during the synthesis process than that the samples especially obtained by the UCP and SCP methods, but the SSAs of the corresponding samples are much smaller than the latter two methods (table 4.2). Judging from the lattice constants shown in the same table, the unit cells of the pure ceria oxides synthesized by different methods vary, but the differences are not very obvious.
Figure 4.11b showed the diffraction patterns of $Ce_{0.5}Fe_{0.5}O_{1.75}$ samples synthesised by sodium hydroxide, citric acid and modified Pechini method, and compared with the pure ceria sample synthesised by SCP method. It can be seen that although the $Ce_{0.5}Fe_{0.5}O_{1.75}$ samples synthesized by these three methods all appeared iron oxide impurity phase compared with pure ceria, the number and intensity of Fe_2O_3 characteristic peaks decreased obviously in the order of SCP > CA > PP. This result is consistent with the literature and our hypothesis: for the various synthesis methods tried in this project, the ability to obtain high homogeneous mixed oxides increases in the order of SCP, CA and PP, while the ability to obtain high specific surface area decreases in this order

4.2 Properties of Rh based catalysts

4.2.1 Characterization results

From the previous results, the samples synthesized by SCP method have higher SSAs and the porous structures are relatively stable at high calcination temperature, so two samples synthesized by SCP method were selected to support Rh and generated 2 wt.% Rh/$Ce_{0.8}Sm_{0.2}O_{1.9}$ and 2 wt.% Rh/$Ce_{0.8}Fe_{0.2}O_{1.9}$ catalysts (represented as 2 wt.% Rh/C80SO and 2 wt.% Rh/C80FO). The catalysts are compared with other Rh/CeO_2 catalysts. The Rh-doped ceria with different Rh molar percentage and synthesis method were also selected as the catalyst for CO_2 methanation reaction. All the samples are calcined at 500 °C. Table 4.3 showed physicochemical properties of the catalysts. The Rh content with weight percentage information was generated from XRF measurement, while the SSAs are measured by N_2-physisorption. The Rh atom dispersion and sizes of supported catalysts are measured by CO-chemisorption technique.

Table 4.3: General properties of Rh based catalysts

Sample Name	Rh content (wt.%)	S_{BET} of support (m^2/g)	S_{BET} of catalyst (m^2/g)	Dispersion (%)	Size (hemisphere) (nm)	Metallic area (m^2/g sample)	Metallic area (m^2/g metal)
2 wt.% Rh/C80SO	1.9	118	109.5	100	1.09	8.87	443.5
2 wt.% Rh/C80FO [1]	1.7	153	140.5	/	/	/	/
1 wt.% Rh/CeO_2	1.0	-	115	109	1.01	4.79	478.83
2 wt.% Rh/CeO_2	1.8	-	118	79	1.40	6.23	346.39
3 wt.% Rh/CeO_2	2.5	-	118	68	1.62	7.45	298.11
C99RO-SCP	0.5	136.3		/	/	/	/
C95RO-SCP	2.9	138.4		/	/	/	/
C95RO-CA1	2.9	50.4		/	/	/	/
C91RO-SCP	5.4	111.1		/	/	/	/

[1]: Sample 2 wt.% Rh/C80FO was skipped since the amount of sample was not enough for CO-chemisorption.

It can be seen from the XRF results that the Rh weight percentage of Rh-loaded catalysts are slightly lower than the aimed value except for 1 wt.% Rh/CeO_2, and the error becomes larger with the increase of loading amount. This error may be caused by the way of calculating the amount of Rh precursor: it was assumed that the precursor $Rh(NO_3)_3$ contains no water molecules, since the chemical didn't rapidly absorb water and dissolve in contact with air during the operation. But in fact, the precursor contains some of water, and may also absorb some water when in contact with air. As a result, errors are generated and expand with increased in use. The problem with Rh loaded CeSmOx sample is that the second order Sm Kα line overlaps with the Rh Kα line. To circumvent this affecting the evaluation the Sm Kα lines were all excluded. The M transitions were used for quantification of Sm instead. This still gave a little error for rhodium, most likely overestimating the content a little.

After loading Rh on C80SO and C80FO, the SSAs of the samples were reduced compared with that before loading. It may be due to a small amount of supported metal are deposited in the pores of C80SO and C80FO, and some of the pores are blocked. For the series of Rh catalysts supported on pure ceria, theoretically,

with the increase of Rh loading, the SSA of the catalyst should decrease. However, the results here show an increase or even an equal phenomenon. This may be due to the error caused by the incomplete drying of the samples before measurement (the samples were all dried at 250 °C for 4 h in a nitrogen flow). To verify this hypothesis, the same samples were dried overnight at the same temperature and nitrogen yielded slightly different results. The SSA of all three catalysts increased, even reaching 129 m^2/g for 1 wt.% Rh/CeO_2, while the SSAs of 2 wt.% Rh/CeO_2 and 3 wt.% Rh/CeO_2 remained the same at 123 m^2/g and did not decrease due to more Rh loadings. The Rh-doped ceria samples have higher SSAs compared with loading Rh catalysts with similar Rh content. This might be due to when doping Rh, the Rh ions were solved into ceria lattice and didn't dispersed in the pores of the cerium oxide surface and block the porous structures.

The Rh dispersion of sample 2 wt.% Rh/C80SO and 1 wt.% Rh/CeO_2 are greater or equal to 100 %, which is unusual. Because when the dispersion is 100 %, it shows that all Rh atoms are surface atoms and can be used for catalysis. In practice, however, the dispersion is less than 100 % due to crystallite growth and intersection. The reason for the Rh dispersion higher than 100 % may be due to the multiple adsorptions of CO on some Rh, or the irreversible adsorption on the pure or Sm-doped ceria support, so that the adsorption stoichiometry CO/Rh may be greater than unity. The metal size (hemisphere) increased with the decrease of dispersion. This proves that the crystallite growth influences the metal dispersion.

4.2.2 Catalytic performance of Rh based catalysts in CO_2 methanation

The prepared Rh-based catalysts are tested in a flow reactor. The catalytic activity of the catalysts for CO_2 methanation (4.1) at different temperatures (150, 250, 350, and 400 °C) in a continuous stream of carbon dioxide was investigated. Hydrogen was fed intermittently, four pulses at each temperature. The composition of CO_2 methanation product was characterized by a mass spectrometer. the carrier gas was Ar with a concentration of 100 %. Figure 4.12 showed an example of mass spectrometry spectra which was generated from catalyst 2 wt.% Rh/C80SO. The mass spectrometry spectra plots for other samples can be checked in appendix A.3

$$CO_2 + 4H_2 = CH_4 + 2H_2O \tag{4.1}$$

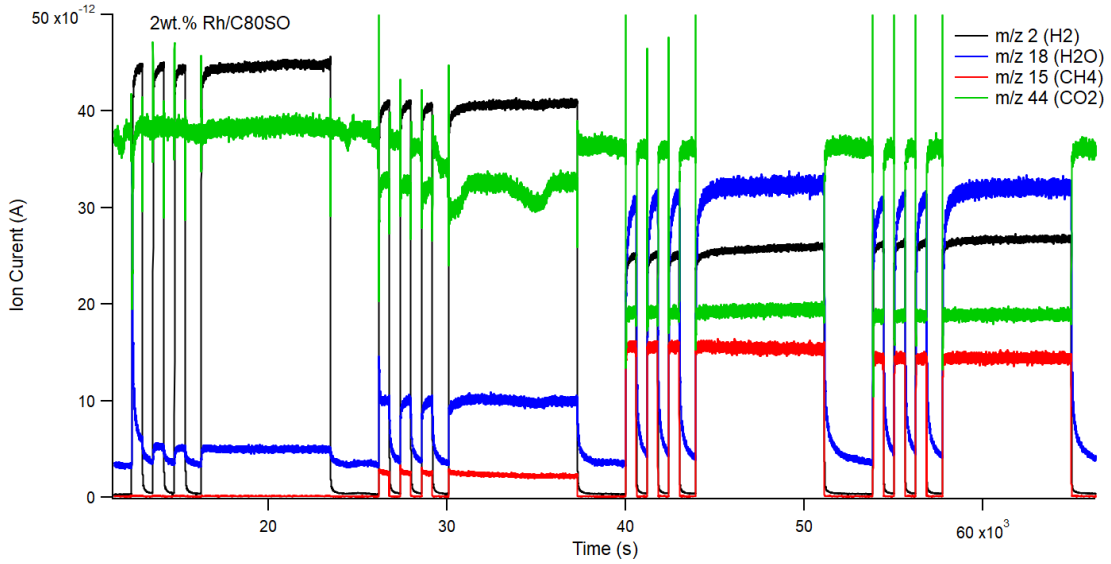

Figure 4.12: Mass spectrometry plot of 2 wt.% Rh/C80SO. The black line represents H_2, green line shows CO_2, blue line refers to H_2O, and the red line related to CH_3^+, which represents methane.

It can be seen from the figure that the reaction of CO_2 hydrogenation began at 250 °C, and a small amount of methane was produced at this temperature. But at 150 °C, when H_2 was flowed in, a small amount of water was produced without the production of methane. It is speculated that H_2O may be generated by combining with oxygen remaining in the reactor or O^{2-} ionized from CO_2 in MS, or it might be the H_2O desorbed from the catalyst surface (there might be some water adsorb on the catalyst and with the increase of temperature, water starts to desorb). The MS spectra of CO_2 fluctuated at 250 °C, which was also seen for other catalysts (appendix A.3). This may be due to fluctuations in the MFC as it regulated the flow. At 350 and 400 °C onset, the reaction rate increased significantly and more methane was produced. From the MS spectra of other catalysts in appendix A.3, it can be seen that from 150 to 400 °C, the catalytic activity of the catalysts increases as the temperature increases. Some catalysts already showed catalytic activity for the CO_2 methanation reaction at 250°C, while C99RO-SCP and C95RO-CA1 did not start showing significant methane production until 350 °C.

The conversion of CO_2 was calculated according to equation 3.11. The results are shown in table 4.4 and figure 4.13. Some of the calculated conversions are negative, this might be the influence of flow regulating by mass flow controllers.

Table 4.4: Conversion of Rh based catalysts at different temperatures

	Conversion (%)			
Sample Name	**150** $°C$	**250** $°C$	**350** $°C$	**400** $°C$
2 wt.% Rh/C80SO	-0.73	12.76	47.86	50.08
2 wt.% Rh/C80FO	-1.28	6.007	22.73	32.61
1 wt.% Rh/CeO_2	0.037	5.32	32.53	38.53
2 wt.% Rh/CeO_2	-2.73	7.324	31.72	37.95
3 wt.% Rh/CeO_2	-1.68	7.24	31.84	35.02
C99RO-SCP	1.883	-1.2	7.357	22.28
C95RO-SCP	4.228	8.916	26.43	34.37
C95RO-CA1	-0.55	0.646	18.58	32.44
C91RO-SCP	2.52	5.358	25.39	30.61

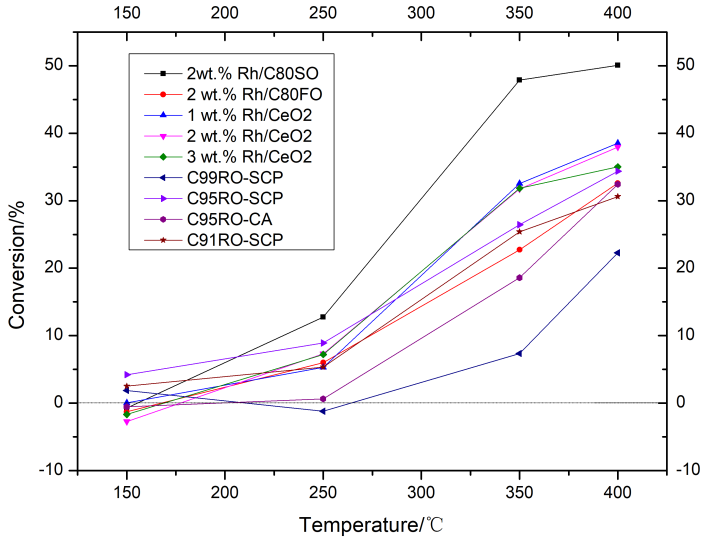

Figure 4.13: Conversion plot of Rh based catalysts at different temperatures (150, 250, 350, and 400 °C). The dashed line represents conversion = 0.

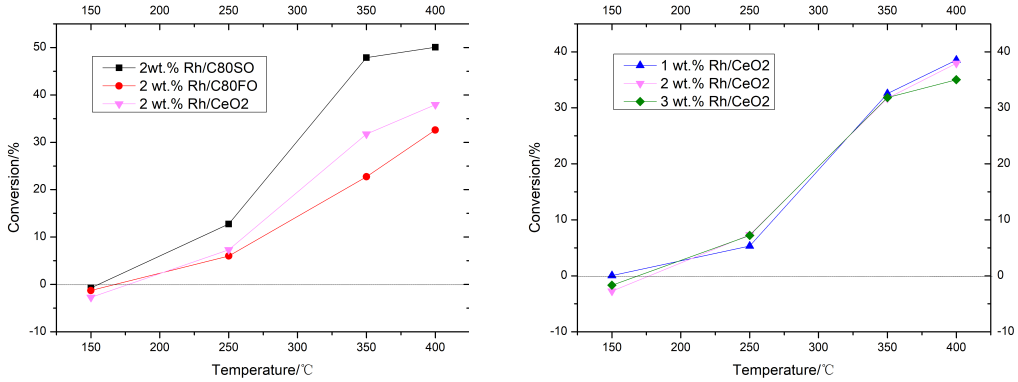

(a) CO_2 conversion comparison of 2 wt.% Rh loading catalysts

(b) CO_2 conversion comparison of 1, 2, 3 wt.% Rh/CeO_2 catalysts

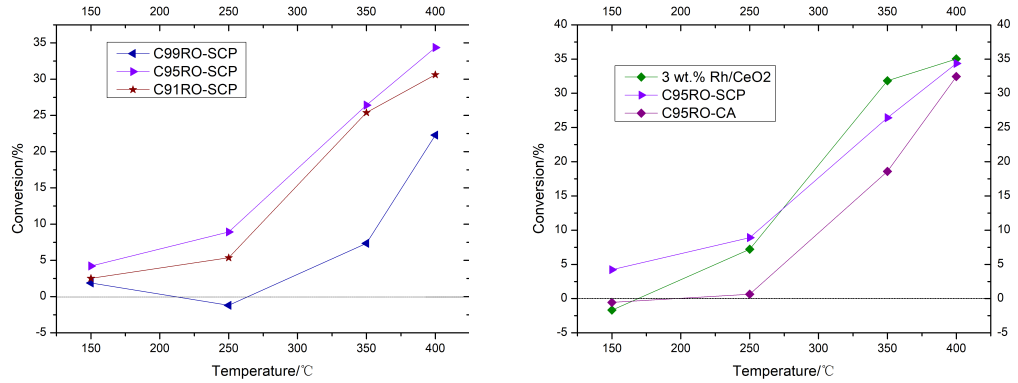

(c) CO_2 conversion comparison of Rh doped ceria synthesised by SCP method

(d) CO_2 conversion comparison of 3 wt.% Rh-based catalysts

Figure 4.14: CO_2 conversion comparison of different catalysts

2 wt.% Rh/C80SO showed the highest CO_2 conversion at 250, 350, and 400 °C among the catalysts, while C99RO-SCP generated the lowest CO_2 conversion at the same temperatures.

Comparing the catalysts with 2 wt.% Rh loading (fig. 4.14a), it seems like the type of support has an influence on the catalytic performance of the Rh based catalysts on CO_2 methanation. The conversion of CO_2 increases in the order of 2 wt.% Rh/C80SO < 2 wt.% Rh/CeO_2 < 2 wt.% Rh/C80SO, which means that doping Sm into ceria helps to improve the catalytic activity of the Rh-based catalyst, while the doping of Fe has a negative effect on the catalytic activity. This also reflects the fact that when the SSAs of the supports are not very different, the type of dopant seems to have a greater impact on the catalyst activity. When the supports are the same, by increasing the loading of Rh, the catalytic performance of Rh/CeO_2 decreased at 400 °C (fig. 4.14b), but in general the CO_2 conversion on the three catalysts are quite similar. For Rh doped ceria synthesised by sodium hydroxide method (fig. 4.14c), when Rh content increase from 0.5 to 5.4 wt. % , the CO_2 conversion first increased and then decreased, catalyst with 2.9 wt.% Rh showed

the best catalytic performance. This may be because of the Rh content is too low, there were not enough CO_2 methanation active sites; and when the Rh content is too high, the SSA of the mixed oxide decreases, and the number of Rh active sites on the oxide surface that can be contacted by the reactive gas decreases. When comparing the catalysts with similar Rh content (around 3 wt.%) but prepared with different method (fig. 4.14d), it can be seen that the one of ceria loading with Rh showed highest CO_2 conversion at 350 and 400 °C. This may be due to that the Rh moiety in CeRhO still exists in the ceria lattice in the form of Rh oxide; and is not transformed into the active site of Rh atoms, so that its catalytic activity is not as high as that of the Rh-supported ceria catalyst. For catalysts C95RO-SCP and C95RO-CA1, they contain the same amount of Rh, but the different synthesis methods of these two catalysts lead to large differences in SSA (138.4 and 50.4 m^2/g). The CO_2 conversion ability of the two catalysts was also proportional to the size of the SSAs.
In general, the type of metal oxide support, the content of Rh loaded on ceria, the way of preparing Rh-doped catalyst as well as the surface area of catalyst all have influence on the catalytic performance of Rh-based catalyst in the aspect of CO_2 conversion,

5

Conclusions

Among all methods used in this project, the sodium hydroxide method performed the best in obtaining metal (Sm, Fe, Rh) doped ceria samples with high specific surface areas, up to 167 m^2/g. The specific surface area results of the samples synthesized by urea method were also good, but compared with the sodium hydroxide method, the SSA of the sample decreased significantly or even halved when the calcination temperature was increased, which proves that the obtained samples are not quite stable. By using the synthesis procedure of sodium hydroxide method and ammonia as the precipitant, the result showed that the precipitant has an influence on the surface area and Na^+ acted as a promoter for generating high SSAs. Even though the modified Pechini method performed the worst in obtaining high surface areas among the 5 methods (with specific surface areas only hovering between 10 and 20 m^2/g), perhaps it can be used in some occasions that do not pursue high SSA but pursue high homogeneity.

From the results of isotherms, the pore structures of different dopant samples synthesized by different methods are very different. For example, the isotherms of the products synthesised by the citric acid method and the modified Pechini method showed a great difference at $pH \approx 1$ and $pH \approx 7$, which proved that the pore structure is significantly dependent on pH. For urea method, the isotherms of the ceria with different dopants are quite different, while for samples synthesised by ammonia and sodium hydroxide method, the dopant doesn't seem to play a role in the porous structures and stabilities. For urea and sodium hydroxide methods, samples with the same composition show a weaker micropore filling phenomenon in the low p/p_0 region at higher calcination temperature, which might be a result of micropores filling caused by particle sintering growth with temperature increase.

The XRD results showed that all methods can be used to synthesize metal-doped ceria with dopant molar content of 0.2 (Sm, Fe) or 0.09 (Rh), and obtain a homogeneous solid solution. Except for the $Ce_{0.8}Fe_{0.2}O_{1.9}$ sample synthesized by urea method and calcined at 500 °C, which showed impurity peaks of α-Fe_2O_3 in XRD pattern. The solubility limit of Sm in ceria in our case is 50 % molar percentage, while for Fe is 40 %. Peak shifts in some samples relative to pure ceria demonstrate that metal ions are doped into the oxide lattice and cause a change in lattice parameter, the calculated lattice constant verified the results. The crystalline size of the products obtained by different methods also varies. The sodium hydroxide method samples, which obtain the highest specific surface areas among the samples in this report, have the lowest crystalline size in general, while the samples obtained by the Pechini method and the citric acid method, which have smaller specific surface areas, have larger crystallines.

The Rh-based catalysts were in a flow reactor with CO_2 methanation reaction. the results showed that most of the catalysts started to be active at 250 °C and producing methane. With the increase of temperature from 150 to 400 °C, the reaction rate increased. Catalyst with Sm-doped ceria support and 2 wt.% Rh loading performed the best in catalyzing CO_2 methanation in this project. It was also found that doping 20 mol.% of Sm into ceria helps boost the catalytic performance of Rh loading catalyst, while doping 20 mol.% of Fe into ceria had a negative effect on catalytic performance. The CO_2 conversion ability of Rh-doped ceria catalysts is in general lower than ceria loading Rh catalysts, and different SSAs of catalysts with same Rh content also showed different catalytic performance.

Bibliography

[1] S. B. Ogale, T. V. Venkatesan, and M. Blamire, *Functional metal oxides: new science and novel applications*. John Wiley & Sons, 2013.

[2] S.-Y. Chen, M. Nishi, A. Chang, W.-C. Hsiao, T. Mochizuki, H. Takagi, and C.-M. Yang, "Well-ordered Cs–Ru/@ SBA-15 nanocomposite materials for low pressure ammonia synthesis," *Sustainable Energy & Fuels*, vol. 4, no. 11, pp. 5802–5811, 2020.

[3] M. Sayehi, H. Tounsi, G. Garbarino, P. Riani, and G. Busca, "Reutilization of silicon-and aluminum-containing wastes in the perspective of the preparation of SiO_2-Al_2O_3 based porous materials for adsorbents and catalysts," *Waste Management*, vol. 103, pp. 146–158, 2020.

[4] N. M. Martin, P. Velin, M. Skoglundh, M. Bauer, and P.-A. Carlsson, "Catalytic hydrogenation of CO_2 to methane over supported Pd, Rh and Ni catalysts," *Catalysis Science & Technology*, vol. 7, no. 5, pp. 1086–1094, 2017.

[5] N. M. Martin, F. Hemmingsson, X. Wang, L. R. Merte, U. Hejral, J. Gustafson, M. Skoglundh, D. M. Meira, A.-C. Dippel, O. Gutowski *et al.*, "Structure–function relationship during CO_2 methanation over Rh/Al_2O_3 and Rh/SiO_2 catalysts under atmospheric pressure conditions," *Catalysis Science & Technology*, vol. 8, no. 10, pp. 2686–2696, 2018.

[6] N. M. Martin, F. Hemmingsson, A. Schaefer, M. Ek, L. R. Merte, U. Hejral, J. Gustafson, M. Skoglundh, A.-C. Dippel, O. Gutowski *et al.*, "Structure–function relationship for CO_2 methanation over ceria supported Rh and Ni catalysts under atmospheric pressure conditions," *Catalysis Science & Technology*, vol. 9, no. 7, pp. 1644–1653, 2019.

[7] K. Malins, "Production of renewable hydrocarbons from vegetable oil refining by-product/waste soapstock over selective sulfur-free high metal loading SiO_2–Al_2O_3 supported Ni catalyst via hydrotreatment," *Journal of Cleaner Production*, vol. 283, p. 125306, 2021.

[8] X. Yan, X.-h. DU, L. Jing, W. Peng, Z. Jie, F.-j. GE, Z. Jun, S. Ming, and W.-y. ZHU, "A comparison of Al_2O_3 and SiO_2 supported Ni-based catalysts in their performance for the dry reforming of methane," *Journal of Fuel Chemistry and Technology*, vol. 47, no. 2, pp. 199–208, 2019.

[9] P. Riani, I. Valsamakis, T. Cavattoni, V. S. Escribano, G. Busca, and G. Gar-

barino, "Ni/SiO_2-Al_2O_3 catalysts for CO_2 methanation: Effect of La_2O_3 addition," *Applied Catalysis B: Environmental*, vol. 284, p. 119697, 2021.

[10] J. Xu, T. Huang, and Y. Fan, "Highly efficient NiMo/SiO_2-Al_2O_3 hydrodesulfurization catalyst prepared from gemini surfactant-dispersed mo precursor," *Applied Catalysis B: Environmental*, vol. 203, pp. 839–850, 2017.

[11] P.-A. Carlsson, M. Skoglundh, E. Fridell, E. Jobson, and B. Andersson, "Induced low temperature catalytic ignition by transient changes in the gas composition," *Catalysis today*, vol. 73, no. 3-4, pp. 307–313, 2002.

[12] P.-A. Carlsson, M. Skoglundh, P. Thormählen, and B. Andersson, "Low-temperature CO oxidation over a Pt/Al_2O_3 monolith catalyst investigated by step-response experiments and simulations," *Topics in catalysis*, vol. 30, no. 1, pp. 375–381, 2004.

[13] P.-A. Carlsson, L. Österlund, P. Thormählen, A. Palmqvist, E. Fridell, J. Jansson, and M. Skoglundh, "A transient in situ FTIR and XANES study of CO oxidation over Pt/Al_2O_3 catalysts," *Journal of Catalysis*, vol. 226, no. 2, pp. 422–434, 2004.

[14] P.-A. Carlsson, V. P. Zhdanov, and M. Skoglundh, "Self-sustained kinetic oscillations in CO oxidation over silica-supported Pt," *Physical Chemistry Chemical Physics*, vol. 8, no. 23, pp. 2703–2706, 2006.

[15] M. Di, K. Simmance, A. Schaefer, Y. Feng, F. Hemmingsson, M. Skoglundh, T. Bell, D. Thompsett, L. I. A. Jensen, S. Blomberg *et al.*, "Chasing PtO_x species in ceria supported platinum during CO oxidation extinction with correlative operando spectroscopic techniques," *Journal of Catalysis*, vol. 409, pp. 1–11, 2022.

[16] P.-A. Carlsson, E. Fridell, and M. Skoglundh, "Methane oxidation over Pt/Al_2O_3 and Pd/Al_2O_3 catalysts under transient conditions," *Catalysis Letters*, vol. 115, no. 1, pp. 1–7, 2007.

[17] S. Fouladvand, M. Skoglundh, and P.-A. Carlsson, "A transient in situ infrared spectroscopy study on methane oxidation over supported pt catalysts," *Catalysis Science & Technology*, vol. 4, no. 10, pp. 3463–3473, 2014.

[18] P. Velin, M. Ek, M. Skoglundh, A. Schaefer, A. Raj, D. Thompsett, G. Smedler, and P.-A. Carlsson, "Water inhibition in methane oxidation over alumina supported palladium catalysts," *The Journal of Physical Chemistry C*, vol. 123, no. 42, pp. 25 724–25 737, 2019.

[19] P. Velin, C.-R. Florén, M. Skoglundh, A. Raj, D. Thompsett, G. Smedler, and P.-A. Carlsson, "Palladium dispersion effects on wet methane oxidation kinetics," *Catalysis Science & Technology*, vol. 10, no. 16, pp. 5460–5469, 2020.

[20] P. Velin, F. Hemmingsson, A. Schaefer, M. Skoglundh, K. A. Lomachenko, A. Raj, D. Thompsett, G. Smedler, and P.-A. Carlsson, "Hampered PdO redox dynamics by water suppresses lean methane oxidation over realistic palladium catalysts," *ChemCatChem*, vol. 13, no. 17, pp. 3765–3771, 2021.

[21] J. Nilsson, P.-A. Carlsson, N. M. Martin, E. C. Adams, G. Agostini, H. Grönbeck, and M. Skoglundh, "Methane oxidation over Pd/Al_2O_3 under rich/lean cycling followed by operando XAFS and modulation excitation spectroscopy," *Journal of Catalysis*, vol. 356, pp. 237–245, 2017.

[22] E. C. Adams, M. Skoglundh, M. Folic, E. C. Bendixen, P. Gabrielsson, and P.-A. Carlsson, "Ammonia formation over supported platinum and palladium catalysts," *Applied Catalysis B: Environmental*, vol. 165, pp. 10–19, 2015.

[23] E. C. Adams, M. Skoglundh, P. Gabrielsson, M. Laurell, and P.-A. Carlsson, "Ammonia formation over Pd/Al_2O_3 modified with cerium and barium," *Catalysis Today*, vol. 267, pp. 210–216, 2016.

[24] E. C. Adams, M. Skoglundh, P. Gabrielsson, and P.-A. Carlsson, "Passive SCR: The effect of H_2 to NO ratio on the formation of NH_3 over alumina supported platinum and palladium catalysts," *Topics in Catalysis*, vol. 59, no. 10, pp. 970–975, 2016.

[25] E. C. Adams, M. Skoglundh, and P.-A. Carlsson, "Ammonia formation from nitric oxide over Pd-based catalysts in multicomponent feed gas compositions," *Catalysis Communications*, vol. 95, pp. 26–30, 2017.

[26] A. L. Karemore, R. Sinha, P. Chugh, and P. D. Vaidya, "Syngas production by carbon dioxide reforming of methane over Pt/Al_2O_3 and Pt/ZrO_2-SiO_2 catalysts," *Chemical Engineering Science*, vol. 249, p. 117347, 2022.

[27] T. ZHENG, H. Junjun, Z. Yunkun, X. Wenzheng, and H. Jieli, "Precious metal-support interaction in automotive exhaust catalysts," *Journal of Rare Earths*, vol. 32, no. 2, pp. 97–107, 2014.

[28] T. Chen, Y.-w. Hu, C. Zhang, and Z.-j. Gao, "Recent progress on transition metal oxides and carbon-supported transition metal oxides as catalysts for thermal decomposition of ammonium perchlorate," *Defence Technology*, vol. 17, no. 4, pp. 1471–1485, 2021.

[29] Y. Jang, Y. H. Lee, H. Eom, S. M. Lee, and S. S. Kim, "Effect of preparation method of noble metal supported catalyts on formaldehyde oxidation at room temperature: Gas or liquid phase reduction," *Journal of Environmental Sciences*, 2022.

[30] Z. Hou, W. Pei, X. Zhang, K. Zhang, Y. Liu, J. Deng, L. Jing, and H. Dai, "Rare earth oxides and their supported noble metals in application of environmental catalysis," *Journal of Rare Earths*, vol. 38, no. 8, pp. 819–839, 2020.

[31] F. M. Pinto, V. Y. Suzuki, R. C. Silva, and F. A. La Porta, "Oxygen defects and surface chemistry of reducible oxides," *Frontiers in Materials*, p. 260, 2019.

[32] P.-A. Carlsson and M. Skoglundh, "Low-temperature oxidation of carbon monoxide and methane over alumina and ceria supported platinum catalysts," *Applied Catalysis B: Environmental*, vol. 101, no. 3-4, pp. 669–675, 2011.

[33] E. Becker, P.-A. Carlsson, and M. Skoglundh, "Methane oxidation over alumina and ceria supported platinum," *Topics in Catalysis*, vol. 52, no. 13, pp. 1957–1961, 2009.

[34] S. Fouladvand, S. Schernich, J. Libuda, H. Grönbeck, T. Pingel, E. Olsson, M. Skoglundh, and P.-A. Carlsson, "Methane oxidation over Pd supported on ceria–alumina under rich/lean cycling conditions," *Topics in Catalysis*, vol. 56, no. 1, pp. 410–415, 2013.

[35] J. Nilsson, P.-A. Carlsson, S. Fouladvand, N. M. Martin, J. Gustafson, M. A. Newton, E. Lundgren, H. Gronbeck, and M. Skoglundh, "Chemistry of supported palladium nanoparticles during methane oxidation," *Acs Catalysis*, vol. 5, no. 4, pp. 2481–2489, 2015.

[36] E. C. Adams, M. Skoglundh, T. Elmøe, and P.-A. Carlsson, "Water–gas-shift assisted ammonia formation over Pd/Ce/alumina," *Catalysis Today*, vol. 307, pp. 169–174, 2018.

[37] F. Hemmingsson, A. Schaefer, M. Skoglundh, and P.-A. Carlsson, "CO_2 methanation over Rh/CeO_2 studied with infrared modulation excitation spectroscopy and phase sensitive detection," *Catalysts*, vol. 10, no. 6, p. 601, 2020.

[38] S. Kattel, W. Yu, X. Yang, B. Yan, Y. Huang, W. Wan, P. Liu, and J. G. Chen, "CO_2 hydrogenation over oxide-supported PtCo catalysts: The role of the oxide support in determining the product selectivity," *Angewandte Chemie International Edition*, vol. 55, no. 28, pp. 7968–7973, 2016.

[39] L. Kylhammar, P.-A. Carlsson, H. H. Ingelsten, H. Grönbeck, and M. Skoglundh, "Regenerable ceria-based SOx traps for sulfur removal in lean exhausts," *Applied Catalysis B: Environmental*, vol. 84, no. 1-2, pp. 268–276, 2008.

[40] A. Ruiz Puigdollers, P. Schlexer, S. Tosoni, and G. Pacchioni, "Increasing oxide reducibility: the role of metal/oxide interfaces in the formation of oxygen vacancies," *Acs Catalysis*, vol. 7, no. 10, pp. 6493–6513, 2017.

[41] Y. Zhang, Y. Xiao, L. Li, K. Song, X. Wang, C. Wang, X. Jian, C. Ji, and P. Qian, "Formaldehyde oxidation on co-doped reduced CeO_2 (111): First-principles calculations," *Surface Science*, vol. 701, p. 121693, 2020.

[42] A. R. Puigdollers, F. Illas, and G. Pacchioni, "Structure and properties of zirconia nanoparticles from density functional theory calculations," *The Journal of Physical Chemistry C*, vol. 120, no. 8, pp. 4392–4402, 2016.

[43] P. Caro, *Rare earths*. Editorial Complutense, 1998.

[44] L. Shuang, W. Xiaodong, W. Duan, and R. Rui, "Ceria-based catalysts for soot oxidation: a review," *Journal of Rare Earths*, vol. 33, no. 6, pp. 567–590, 2015.

[45] X. Wang, J. A. Rodriguez, J. C. Hanson, D. Gamarra, A. Martínez-Arias, and M. Fernández-García, "In situ studies of the active sites for the water gas

shift reaction over Cu–CeO_2 catalysts: complex interaction between metallic copper and oxygen vacancies of ceria," *The Journal of Physical Chemistry B*, vol. 110, no. 1, pp. 428–434, 2006.

[46] S. Dey and G. C. Dhal, "Cerium catalysts applications in carbon monoxide oxidations," *Materials Science for Energy Technologies*, vol. 3, pp. 6–24, 2020.

[47] W. Yang, X. Wang, S. Song, and H. Zhang, "Syntheses and applications of noble-metal-free CeO_2-based mixed-oxide nanocatalysts," *Chem*, vol. 5, no. 7, pp. 1743–1774, 2019.

[48] S. R. Mishra and M. Ahmaruzzaman, "Cerium oxide and its nanocomposites: Structure, synthesis, and wastewater treatment applications," *Materials Today Communications*, p. 102562, 2021.

[49] R. Li, S. Yabe, M. Yamashita, S. Momose, S. Yoshida, S. Yin, and T. Sato, "Synthesis and UV-shielding properties of ZnO-and CaO-doped CeO_2 via soft solution chemical process," *Solid State Ionics*, vol. 151, no. 1-4, pp. 235–241, 2002.

[50] P. Janoš, J. Ederer, V. Pilařová, J. Henych, J. Tolasz, D. Milde, and T. Opletal, "Chemical mechanical glass polishing with cerium oxide: Effect of selected physico-chemical characteristics on polishing efficiency," *Wear*, vol. 362, pp. 114–120, 2016.

[51] M. M. Khan, S. A. Ansari, D. Pradhan, D. H. Han, J. Lee, and M. H. Cho, "Defect-induced band gap narrowed CeO_2 nanostructures for visible light activities," *Industrial & Engineering Chemistry Research*, vol. 53, no. 23, pp. 9754–9763, 2014.

[52] N. J. Lawrence, J. R. Brewer, L. Wang, T.-S. Wu, J. Wells-Kingsbury, M. M. Ihrig, G. Wang, Y.-L. Soo, W.-N. Mei, and C. L. Cheung, "Defect engineering in cubic cerium oxide nanostructures for catalytic oxidation," *Nano letters*, vol. 11, no. 7, pp. 2666–2671, 2011.

[53] T. Montini, M. Melchionna, M. Monai, and P. Fornasiero, "Fundamentals and catalytic applications of CeO_2-based materials," *Chemical reviews*, vol. 116, no. 10, pp. 5987–6041, 2016.

[54] P. Li, Y. Xin, Q. Li, Z. Wang, Z. Zhang, and L. Zheng, "Ce–Ti amorphous oxides for selective catalytic reduction of NO with NH_3: confirmation of Ce–O–Ti active sites," *Environmental science & technology*, vol. 46, no. 17, pp. 9600–9605, 2012.

[55] M. Y. Mihaylov, E. Z. Ivanova, G. N. Vayssilov, and K. I. Hadjiivanov, "Revisiting ceria-NO_x interaction: FTIR studies," *Catalysis Today*, vol. 357, pp. 613–620, 2020.

[56] Y. Shan, Y. Liu, Y. Li, and W. Yang, "A review on application of cerium-based oxides in gaseous pollutant purification," *Separation and Purification Technology*, vol. 250, p. 117181, 2020.

[57] Y. Ma, W. Gao, Z. Zhang, S. Zhang, Z. Tian, Y. Liu, J. C. Ho, and Y. Qu, "Regulating the surface of nanoceria and its applications in heterogeneous catalysis," *Surface Science Reports*, vol. 73, no. 1, pp. 1–36, 2018.

[58] A. Trovarelli, *Catalysis by ceria and related materials*. World Scientific, 2002, vol. 2.

[59] D. Das, S. Gupta, and K. Sudarshan, "Europium luminescence as a structural probe to understand defect evolution in CeO_2/Eu^{3+}, M^{3+} (M= Y and La): contrasting role of codopant ionic size," *Journal of Materials Science*, vol. 56, no. 30, pp. 17 205–17 220, 2021.

[60] D. Devaiah, L. H. Reddy, S.-E. Park, and B. M. Reddy, "Ceria–zirconia mixed oxides: Synthetic methods and applications," *Catalysis Reviews*, vol. 60, no. 2, pp. 177–277, 2018.

[61] E. Aneggi, C. de Leitenburg, G. Dolcetti, and A. Trovarelli, "Diesel soot combustion activity of ceria promoted with alkali metals," *Catalysis Today*, vol. 136, no. 1-2, pp. 3–10, 2008.

[62] K. Liu, X. Xu, J. Xu, X. Fang, L. Liu, and X. Wang, "The distributions of alkaline earth metal oxides and their promotional effects on Ni/CeO_2 for CO_2 methanation," *Journal of CO2 Utilization*, vol. 38, pp. 113–124, 2020.

[63] R. Kırkgeçit, H. Ö. Torun, F. K. Dokan, and E. Öztürk, "Investigation of optic and electrical conductivity properties of rare earth elements (Sm, Y, La, Er) co-doped CeO_2," *Journal of Rare Earths*, 2021.

[64] I. V. Zagaynov, I. V. Shelepin, S. V. Fedorov, A. V. Naumkin, A. V. Bykov, and A. A. Konovalov, "Sm (Nd) doped ceria materials for multifunctional application," *Ceramics International*, vol. 47, no. 15, pp. 22 201–22 208, 2021.

[65] A. A. AlKhoori, K. Polychronopoulou, A. Belabbes, M. Abi Jaoude, L. F. Vega, V. Sebastian, S. Hinder, M. A. Baker, and A. F. Zedan, "Cu, Sm co-doping effect on the CO oxidation activity of CeO_2. a combined experimental and density functional study," *Applied Surface Science*, vol. 521, p. 146305, 2020.

[66] G. Siakavelas, N. Charisiou, A. AlKhoori, S. AlKhoori, V. Sebastian, S. Hinder, M. Baker, I. Yentekakis, K. Polychronopoulou, and M. Goula, "Highly selective and stable Ni/La-M (M= Sm, Pr, and Mg)-CeO_2 catalysts for CO_2 methanation," *Journal of CO2 Utilization*, vol. 51, p. 101618, 2021.

[67] J. Wang, M. Shen, J. Wang, M. Cui, J. Gao, J. Ma, and S. Liu, "Preparation of $Fe_xCe_{1-x}O_y$ solid solution and its application in Pd-only three-way catalysts," *Journal of Environmental Sciences*, vol. 24, no. 4, pp. 757–764, 2012.

[68] H. Bao, X. Chen, J. Fang, Z. Jiang, and W. Huang, "Structure-activity relation of Fe_2O_3–CeO_2 composite catalysts in CO oxidation," *Catalysis letters*, vol. 125, no. 1, pp. 160–167, 2008.

[69] O. Laguna, M. Centeno, G. Arzamendi, L. Gandía, F. Romero-Sarria, and

J. A. Odriozola, "Iron-modified ceria and Au/ceria catalysts for total and preferential oxidation of CO (TOX and PROX)," *Catalysis today*, vol. 157, no. 1-4, pp. 155–159, 2010.

[70] M. O. Mazan, J. Marrero-Jerez, A. Soldati, P. Nunez, and S. A. Larrondo, "Fe-doped ceria nanopowders synthesized by freeze-drying precursor method for electrocatalytic applications," *International Journal of Hydrogen Energy*, vol. 40, no. 10, pp. 3981–3989, 2015.

[71] A. Kaftan, F. Kollhoff, T.-S. Nguyen, L. Piccolo, M. Laurin, and J. Libuda, "Sensitivity of CO oxidation toward metal oxidation state in ceria-supported catalysts: an operando drifts-ms study," *Catalysis Science & Technology*, vol. 6, no. 3, pp. 818–828, 2016.

[72] M. Fernandez-Garcia and J. Anderson, "Supported metals in catalysis, catalytic sciences series, vol. 5," 2005.

[73] P. Bera and M. Hegde, "Noble metal ions in CeO_2 and TiO_2: Synthesis, structure and catalytic properties," *RSC advances*, vol. 5, no. 115, pp. 94 949–94 979, 2015.

[74] W. Zhang, G. Zhang, C. Liu, J. Li, T. Zheng, J. Ma, L. Wang, J. Jiang, and X. Zhai, "Enhanced removal of arsenite and arsenate by a multifunctional Fe-Ti-Mn composite oxide: photooxidation, oxidation and adsorption," *Water research*, vol. 147, pp. 264–275, 2018.

[75] G.-Y. ADACHI and T. MASUI, "Synthesis and modification of ceria-based materials," in *Catalysis by Ceria and Related Materials*. World Scientific, 2002, pp. 51–83.

[76] N. Guillén-Hurtado, I. Atribak, A. Bueno-López, and A. García-García, "Influence of the cerium precursor on the physico-chemical features and NO to NO_2 oxidation activity of ceria and ceria–zirconia catalysts," *Journal of Molecular Catalysis A: Chemical*, vol. 323, no. 1-2, pp. 52–58, 2010.

[77] D. Jampaiah, K. M. Tur, S. J. Ippolito, Y. M. Sabri, J. Tardio, S. K. Bhargava, and B. M. Reddy, "Structural characterization and catalytic evaluation of transition and rare earth metal doped ceria-based solid solutions for elemental mercury oxidation," *RSC advances*, vol. 3, no. 31, pp. 12 963–12 974, 2013.

[78] F. Charbgoo, M. Ramezani, and M. Darroudi, "Bio-sensing applications of cerium oxide nanoparticles: advantages and disadvantages," *Biosensors and Bioelectronics*, vol. 96, pp. 33–43, 2017.

[79] F. Lin, A. Wokaun, and I. Alxneit, "Rh-doped ceria: solar organics from H_2O, CO_2 and sunlight?" *Energy Procedia*, vol. 69, pp. 1790–1799, 2015.

[80] D. Bokov, A. Turki Jalil, S. Chupradit, W. Suksatan, M. Javed Ansari, I. H. Shewael, G. H. Valiev, and E. Kianfar, "Nanomaterial by sol-gel method: Synthesis and application," *Advances in Materials Science and Engineering*, vol. 2021, 2021.

[81] R. Jacot, R. Moré, R. Michalsky, A. Steinfeld, and G. R. Patzke, "Trends in the phase stability and thermochemical oxygen exchange of ceria doped with potentially tetravalent metals," *Journal of Materials Chemistry A*, vol. 5, no. 37, pp. 19 901–19 913, 2017.

[82] Y.-f. Bu, Q. Zhong, W.-y. Tan, R.-j. Zhou, Y. Song, and W. Cai, "Synthesis and properties of samaria-doped ceria electrolyte via ultrasound–microwave assisted sol–gel method," *Materials science in semiconductor processing*, vol. 16, no. 6, pp. 2058–2062, 2013.

[83] M. P. Pechini, "Method of preparing lead and alkaline earth titanates and niobates and coating method using the same to form a capacitor," Jul. 11 1967, uS Patent 3,330,697.

[84] T. O. L. Sunde, T. Grande, and M.-A. Einarsrud, "Modified pechini synthesis of oxide powders and thin films," *Handbook of sol-gel science and technology*, 2016.

[85] M. Kakihana and M. Yoshimura, "Synthesis and characteristics of complex multicomponent oxides prepared by polymer complex method," *Bulletin of the Chemical Society of Japan*, vol. 72, no. 7, pp. 1427–1443, 1999.

[86] L. B. Winck, J. L. de Almeida Ferreira, J. M. G. Martinez, J. A. Araujo, A. C. M. Rodrigues, and C. R. M. da Silva, "Synthesis, sintering and characterization of ceria-based solid electrolytes codoped with samaria and gadolinium using the pechini method," *Ceramics International*, vol. 43, no. 18, pp. 16 408–16 415, 2017.

[87] N. Cioateră, V. Pârvulescu, A. Rolle, and R. Vannier, "Enhanced ionic conductivity of Sm, Gd-doped ceria induced by modification of powder synthesis procedure," *Ceramics International*, vol. 38, no. 7, pp. 5461–5468, 2012.

[88] B. Bochentyn, D. Szymczewska, T. Miruszewski, S.-F. Wang, and P. Jasiński, "The influence of synthesis method on the microstructure and catalytic performance of $Y_{0.07}Sr_{0.93}Ti_{0.8}Fe_{0.2}O_{3-\delta}$ in synthetic biogas operated solid oxide fuel cells," *Materials Research Bulletin*, vol. 100, pp. 49–55, 2018.

[89] I. Moog, C. Feral-Martin, M. Duttine, A. Wattiaux, C. Prestipino, S. Figueroa, J. Majimel, and A. Demourgues, "Local organization of Fe^{3+} into nano-CeO_2 with controlled morphologies and its impact on reducibility properties," *Journal of Materials Chemistry A*, vol. 2, no. 47, pp. 20 402–20 414, 2014.

[90] E. Derevyannikova, T. Y. Kardash, L. Kibis, E. Slavinskaya, V. Svetlichnyi, O. Stonkus, A. Ivanova, and A. Boronin, "The structure and catalytic properties of Rh-doped CeO_2 catalysts," *Physical Chemistry Chemical Physics*, vol. 19, no. 47, pp. 31 883–31 897, 2017.

[91] M. Kosinski, A. Vizcaíno, L. Gómez-Sainero, A. Carrero, and R. Baker, "Methanol reforming by nanostructured Pd/Sm-doped ceria catalysts," *Applied Catalysis B: Environmental*, vol. 286, p. 119935, 2021.

[92] I. H. Lone, J. Aslam, N. R. Radwan, A. Akhter, A. H. Bashal, and R. A. Shiekh, "Review on polymeric citrate precursor and sono-chemical methods for the synthesis of nanomaterials," *Current Analytical Chemistry*, vol. 16, no. 7, pp. 826–832, 2020.

[93] A. N. Alexandrova and W. L. Jorgensen, "Why urea eliminates ammonia rather than hydrolyzes in aqueous solution," *The Journal of Physical Chemistry B*, vol. 111, no. 4, pp. 720–730, 2007.

[94] N. Wen and M. H. Brooker, "Rate constants for cyanate hydrolysis to urea: A raman study," *Canadian journal of chemistry*, vol. 72, no. 4, pp. 1099–1106, 1994.

[95] R. R. Rajaram, J. W. Hayes, G. P. Ansell, and H. A. Hatcher, "Catalyst," Jan. 2 1996, uS Patent 5,480,854.

[96] P. Jana, A. Víctor, J. M. Coronado, D. P. Serrano *et al.*, "Cobalt based catalysts prepared by pechini method for CO_2-free hydrogen production by methane decomposition," *International journal of hydrogen energy*, vol. 35, no. 19, pp. 10 285–10 294, 2010.

[97] M. Thommes, K. Kaneko, A. V. Neimark, J. P. Olivier, F. Rodriguez-Reinoso, J. Rouquerol, and K. S. Sing, "Physisorption of gases, with special reference to the evaluation of surface area and pore size distribution (IUPAC technical report)," *Pure and applied chemistry*, vol. 87, no. 9-10, pp. 1051–1069, 2015.

[98] L. Dimesso, "Pechini processes: an alternate approach of the sol–gel method, preparation, properties, and applications," *Handbook of Sol-Gel Science and Technology*, vol. 2, pp. 1–22, 2016.

[99] K. A. Cychosz and M. Thommes, "Progress in the physisorption characterization of nanoporous gas storage materials," *Engineering*, vol. 4, no. 4, pp. 559–566, 2018.

[100] R. A. Sheldon and R. A. Van Santen, *Catalytic Oxidation: Principles And Applications-A Course Of The Netherlands Institute For Catalysis Research (Niok)*. World Scientific, 1995.

[101] T. Sochi, "High throughput software for powder diffraction and its application to heterogeneous catalysis," *arXiv preprint arXiv:1012.4506*, 2010.

[102] F. Hemmingsson, *Transient in Situ Studies on Supported Catalysts: CO_2 Methanation and Methane Oxidation*. Chalmers Tekniska Hogskola (Sweden), 2021.

[103] J.-h. Yi, F.-q. Zhao, H.-x. Gao, S.-y. XU, R.-z. HU, and Y. WANG, "Decomposition mechanism and non-isothermal reaction kinetics of cerium citrate," *CHINESE JOURNAL OF EXPLOSIVES AND PROPELLANTS*, vol. 30, no. 4, p. 1, 2007.

A

Appendix 1

A.1 Sample information

Table A.1: Sample information for metal oxides

NO.	Sample Name	Dopant	Composition	Synthesis Method	Calcine Temperature (°C)	Drying method	S_{BET} (m^2/g)	Lattice Constant (a)(Å)	D_{XRD} (nm)
1	C80SO-ACP-F500	Sm	0.8:0.2	ACP	500	Freeze drying for 2 days	37.8	5.43002	9.38
2	C80SO-CA1-F500	Sm	0.8:0.2	CA1	500	oven drying at 110 °C for 16h	7.41	5.43554	10.95
3	C80SO-CA7-F500	Sm	0.8:0.2	CA7	500	oven drying at 110 °C 200°C for 24h	25.6	5.43965	11.57
4	C80SO-CA7-F500	Sm	0.8:0.2	CA7	500	Dried on heating plate at 201 °C for 4h	33.3	5.43341	11.01
5	C80FO-ACP-F500	Fe	0.8:0.2	ACP	500	Freeze drying for 2 days	46.9	5.39384	8.05
6	CeO2-ACP-F500	/	1.0:0	ACP	500	Freeze drying for 2 days	49.4	5.40786	11.49
7	CeO2-CA7-F500	/	1.0:0	CA7	500	Dried on heating plate at 201 °C for 4.5h	25.6	5.4082	14.37
8	C80SO-PP-F500	Sm	0.8:0.2	PP	500	oven drying at 110 °C for 18h	15.4	5.42971	12.97
9	CeO2-CA1-F150,500	/	1.0:0	CA1	150 and 500	oven drying at 110 °C for 14h	3.57	5.41074	24.54
10	CeO2-PP-F500	/	1.0:0	PP	500	Dried on heating plate at 201 °C for 5h	19.9	5.40933	16.49
11	C80FO-CA1-F500	Fe	0.8:0.2	CA1	500	Dried on heating plate at 201 °C for 5h	36.7	5.38681	4.97
12	C80SO-UCP-F350	Sm	0.8:0.2	UCP	350	Freeze drying for 1 day	86.8	5.43625	5.28
	C80SO-UCP-F500	Sm	0.8:0.2	UCP	500	Freeze drying for 1 day	43.17	5.43533	7.56
13	C80FO-PP-F500	Fe	0.8:0.2	PP	500	Dried on heating plate at 201 °C for 5h	13.3	5.38843	4.33
14	CeO2-UCP-F350	/	1.0:0	UCP	350	Oven drying at 100 °C for 10h	125.6	5.41478	6.02
	CeO2-UCP-F500	/	1.0:0	UCP	500	Oven drying at 100 °C for 10h	78.1	5.41116	8.26
15	C80FO-UCP-F350	Fe	0.8:0.2	UCP	350	Oven drying at 100 °C for 10h	95.2	5.41149	6.33
	C80FO-UCP-F500	Fe	0.8:0.2	UCP	500	Oven drying at 100 °C for 10h	66	5.39789	5.69
16	C80SO-SCP-F350	Sm	0.8:0.2	SCP	350	Oven drying at 110 °C for 12h	135	5.42702	4.85
	C80SO-SCP-F500	Sm	0.8:0.2	SCP	500	Oven drying at 110 °C for 12h	108.7	5.42455	5.31
17	C80FO-SCP-F350	Fe	0.8:0.2	SCP	350	Oven drying at 110 °C for 12h	118.9	5.37103	4.72
	C80FO-SCP-F500	Fe	0.8:0.2	SCP	500	Oven drying at 110 °C for 12h	92.7	5.37132	4.94
18	C80FO-CA7-F500	Fe	0.8:0.2	CA7	500	Dried on the heating plate at 201 °C for 5h	30.5	5.39171	6.37
19	C80SO-UCP-F350	Sm	0.8:0.2	UCP	350	Oven drying at 100 °C for 10h	71.5	5.43040	6.19
	C80SO-UCP-F500	Sm	0.8:0.2	UCP	500	Oven drying at 100 °C for 10h	29.1	5.42958	9.67
20	C985PO-SCP-F350	Pt	0.985:0.015	SCP	350	Oven drying at 110 °C for 12h	143.1	5.40425	4.75
	C985PO-SCP-F500	Pt	0.985:0.015	SCP	500	Oven drying at 110 °C for 12h	130.7	5.40875	5.04
21	C95RO-SCP-F350	Rh	0.95:0.05	SCP	350	Oven drying at 110 °C for 12h	156.9	5.39999	4.31
	C95RO-SCP-F500	Rh	0.95:0.05	SCP	500	Oven drying at 110 °C for 12h	138.4	5.39876	4.64
22	CeO2-SCP-F350	/	1.0:0	SCP	350	Oven drying at 110 °C for 12h	165	5.39486	4.32
	CeO2-SCP-F500	/	1.0:0	SCP	500	Oven drying at 110 °C for 12h	121.5	5.40432	5.10
23	C97PO-CA1-F500	Pt	0.97:0.03	CA1	500	Dried on the heating plate at 201 °C for 5h	28.8	5.41170	7.66
24	C95RO-CA1-F500	Rh	0.95:0.05	CA1	500	Dried on the heating plate at 201 °C for 5h	50.4	5.40645	5.81
25	C80SO-ACP-F350	Sm	0.8:0.2	ACP(precursor to ammonia)	350	Oven drying at 110 °C for 12h	68		
	C80SO-ACP-F500	Sm	0.8:0	ACP(precursor to ammonia)	500	Oven drying at 110 °C for 12h	12		
26	C50SO-SCP-F350	Sm	0.5:0.5	SCP	350	Oven drying at 110 °C for 12h	127	5.44814	5.03
27	C50FO-SCP-F350	Fe	0.5:0.5	SCP	350	Oven drying at 110 °C for 12h	136	6.75457	5.01
	C50FO-SCP-F500	Fe	0.5:0.5	SCP	500	Oven drying at 110 °C for 12h	54.8	-	-
28	C60SO-SCP-F350	Sm	0.6:0.4	SCP	350	Oven drying at 110 °C for 12h	136	5.44278	4.86
29	C60FO-SCP-F350	Fe	0.6:0.4	SCP	350	Oven drying at 110 °C for 12h	137	5.97	3.72
30	C97PO-SCP-F350	Pt	0.97:0.03	SCP	350	Oven drying at 110 °C for 12h	158	5.40499	4.64
31	C91RO-SCP-F350	Rh	0.91:0.09	SCP	350	Oven drying at 110 °C for 12h	120.6	5.39751	5.01
	C91RO-SCP-F500	Rh	0.91:0.09	SCP	500	Oven drying at 110 °C for 12h	111.1		
32	C99RO-SCP-F350	Rh	0.99:0.01	SCP	350	Oven drying at 110 °C for 12h	154.8	5.40107	4.41
	C99RO-SCP-F500	Rh	0.99:0.01	SCP	500	Oven drying at 110 °C for 12h	136.3		
33	Sm2O3-SCP-F350	-	0:1	SCP	350	Oven drying at 110 °C for 12h	102		
34	C50FO-CA1-F500	Fe	0.5:0.5	CA1	500	Dried on heating plate at 201 °C for 5h	31.9	5.92061	4.51
35	C50FO-PP-F500	Fe	0.5:0.5	PP	500	Dried on heating plate at 201 °C for 5h	13.3	5.34103	4.26
36	C80SO-SCP-F500	Sm	0.8:0.2	SCP	500	Oven drying at 110 °C for 12h	118	5.41992	5.25
37	C60SO-SCP-F500	Sm	0.6:0.4	SCP	500	Oven drying at 110 °C for 12h	108.8	5.44269	5.34
38	C80FO-SCP-F500	Fe	0.8:0.2	SCP	500	Oven drying at 110 °C for 12h	153	5.39221	4.32

ACP - Co-precipitation with ammonia (Ammonia method);
UCP - Co-precipitation with urea (Urea method);
SCP - Co-precipitation with sodium hydroxide (Sodium hydroxide method);
CA1- Citric acid method ($pH \approx 1$);
CA7- Citric acid method ($pH \approx 7$);
PP- Modified Pechini method;
F150 - calcination temperature = 150 °C;
F350 - calcination temperature = 350 °C;
F500 - calcination temperature = 500 °C;

A.2 Isotherms for all the samples

A.2.1 Ammonia method

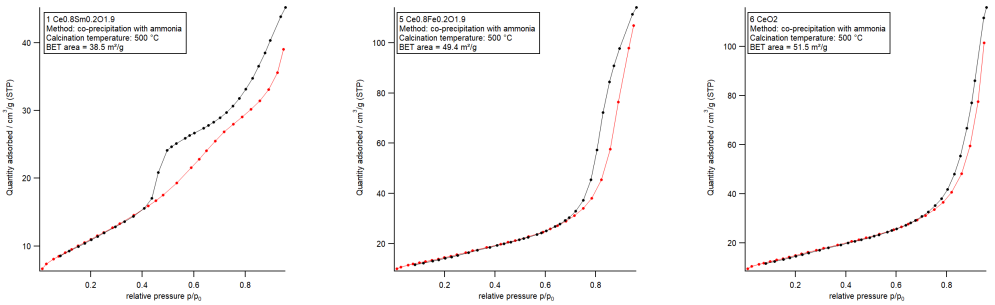

(a) 5 C80FO-ACP-F500 **(b)** 5 C80FO-ACP-F500 **(c)** 6 CeO_2-ACP-F500

Figure A.1: Isotherms for ammonia method samples

A.2.2 Urea method

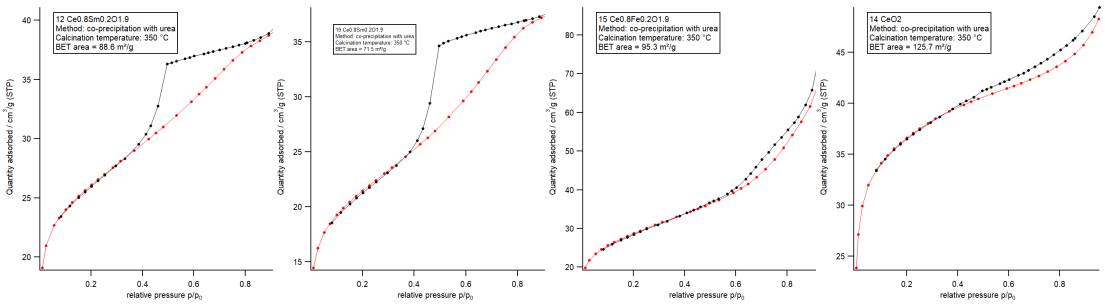

(a) 12 C80SO-UCP-F350 **(b)** 19 C80SO-UCP-F350 **(c)** 15 C80FO-UCP-F350 **(d)** 14 CeO_2-UCP-F350

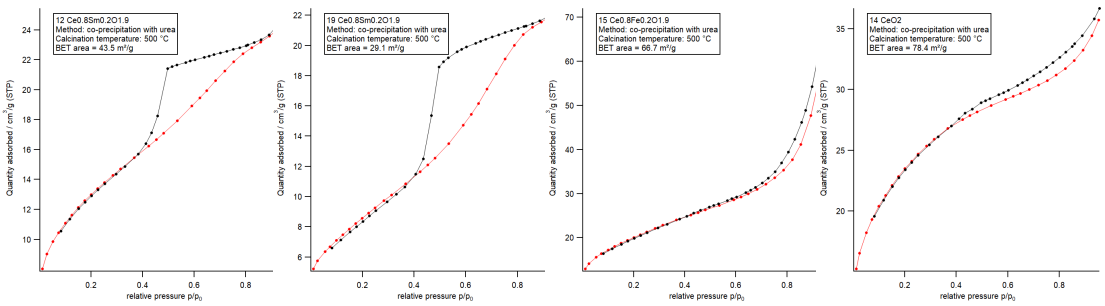

(e) 12 C80SO-UCP-F500 **(f)** 19 C80SO-UCP-F500 **(g)** 15 C80FO-UCP-F500 **(h)** 14 CeO_2-UCP-F500

Figure A.2: Isotherms for urea method samples

A.2.3 Sodium hydroxide method

Pure CeO_2 and Sm_2O_3

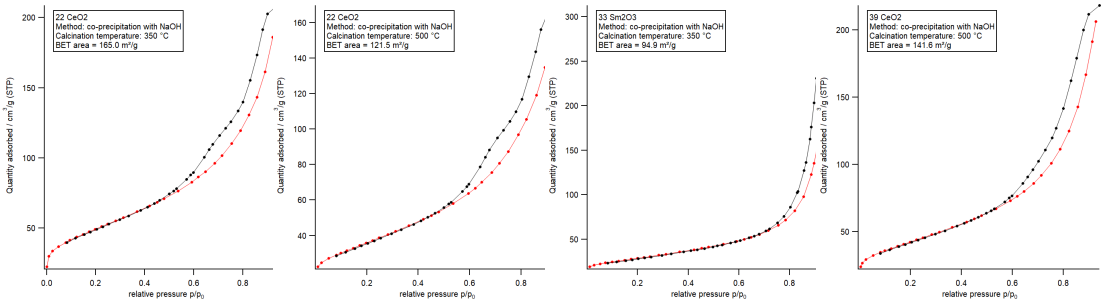

(a) 22 CeO_2-SCP-F350 **(b)** 22 CeO_2-SCP-F500 **(c)** 33 Sm_2O_3-SCP-F350 **(d)** 39 CeO_2-SCP-F500

Figure A.3: Isotherms for sodium hydroxide method pure CeO_2 and Sm_2O_3 samples

Sm-doped ceria

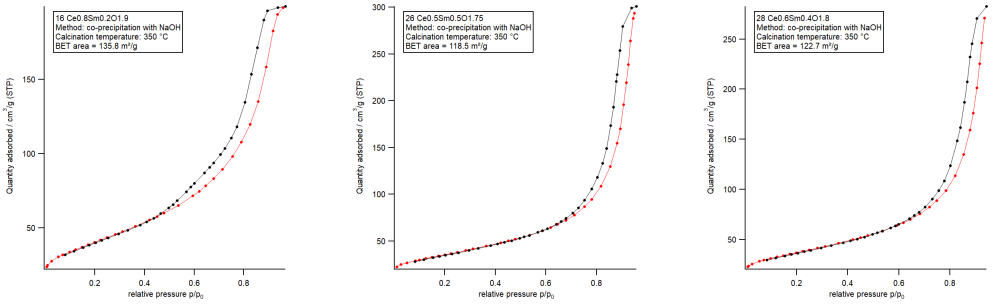

(a) 16 C80SO-SCP-F350 **(b)** 26 C50SO-SCP-F350 **(c)** 28 C60SO-SCP-F350

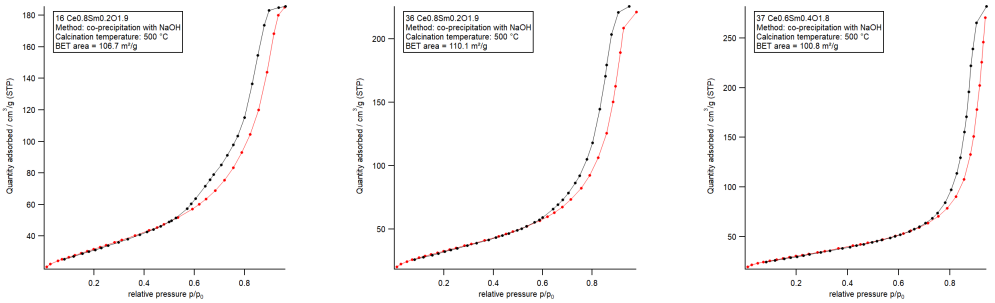

(d) 16 C80SO-SCP-F500 **(e)** 36 C80SO-SCP-F500 **(f)** 37 C60SO-SCP-F500

Figure A.4: Isotherms for sodium hydroxide method Sm-doped ceria samples

Fe-doped ceria

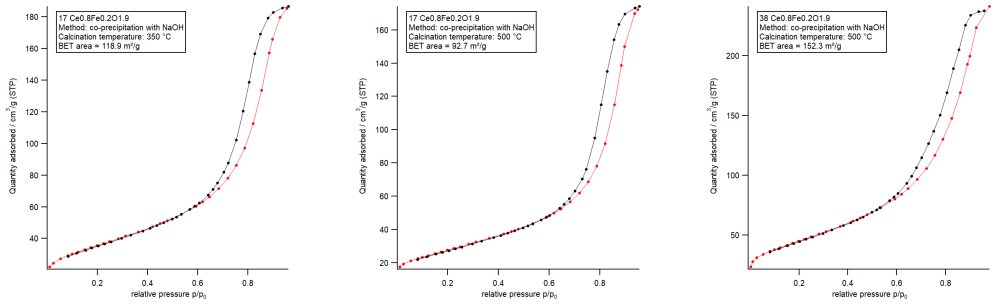

(a) 17 C80FO-SCP-F350 **(b)** 17 C80FO-SCP-F500 **(c)** 38 C80FO-SCP-F500

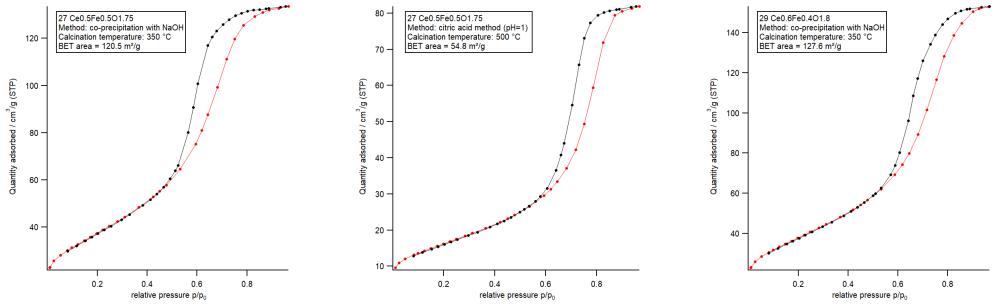

(d) 27 C50FO-SCP-F350 **(e)** 27 C50FO-SCP-F500 **(f)** 29 C60FO-SCP-F350

Figure A.5: Isotherms for sodium hydroxide method Fe-doped ceria samples

Pt-doped ceria

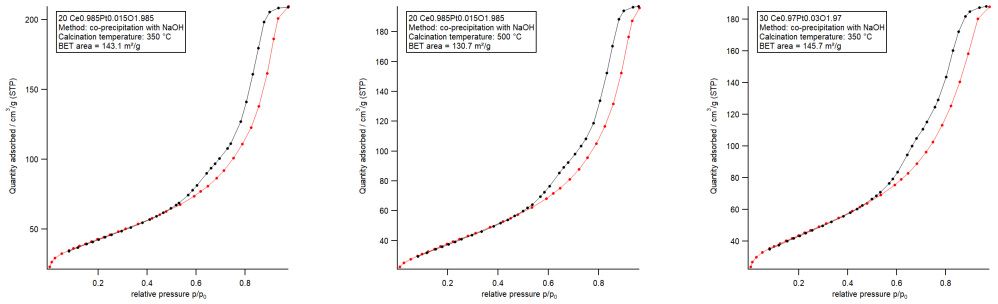

(a) 20 C985PO-SCP-F350 **(b)** 20 C985PO-SCP-F500 **(c)** 30 C97PO-SCP-F350

Figure A.6: Isotherms for sodium hydroxide method Pt-doped ceria samples

Rh-doped ceria

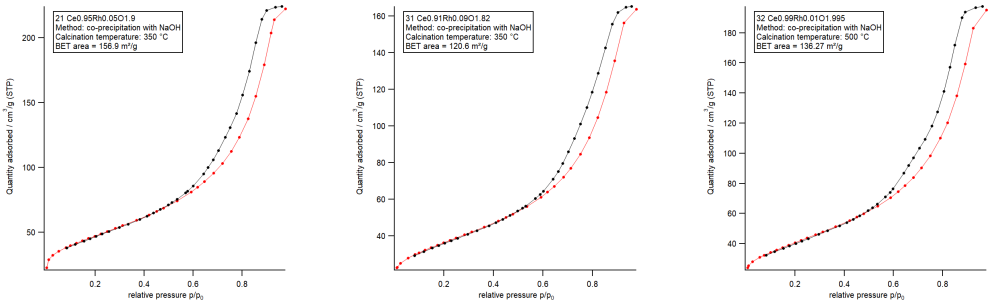

(a) 21 C95RO-SCP-F350 **(b)** 31 C91RO-SCP-F350 **(c)** 32 C99RO-SCP-F350

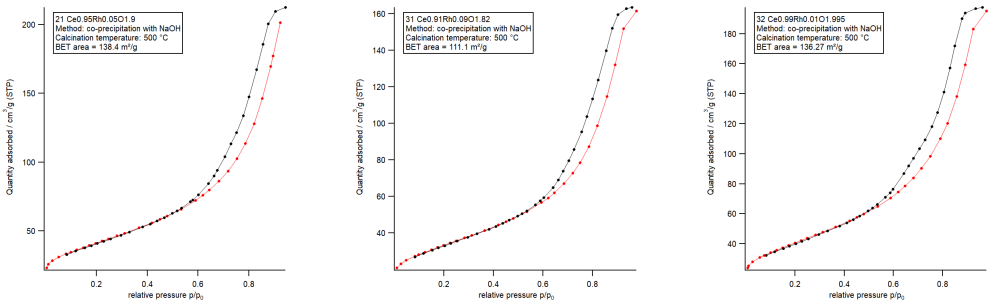

(d) 21 C95RO-SCP-F500 **(e)** 31 C91RO-SCP-F500 **(f)** 32 C99RO-SCP-F500

Figure A.7: Isotherms for sodium hydroxide method Rh-doped ceria samples

A.2.4 Citric acid method

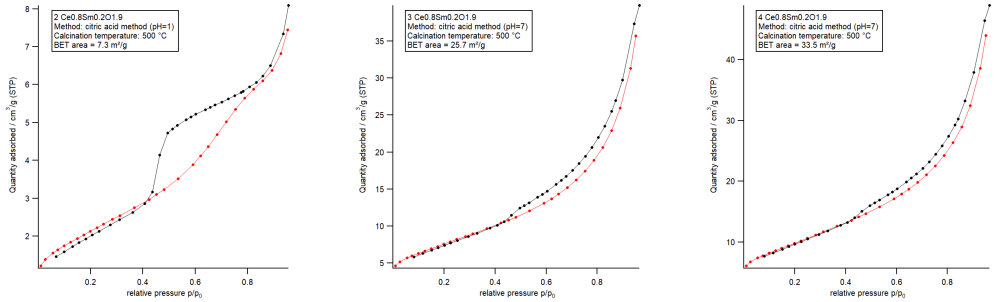

(a) 2 C80SO-CA1-F500 **(b)** 3 C80SO-CA7-F500 **(c)** 4 C80SO-CA7-F500

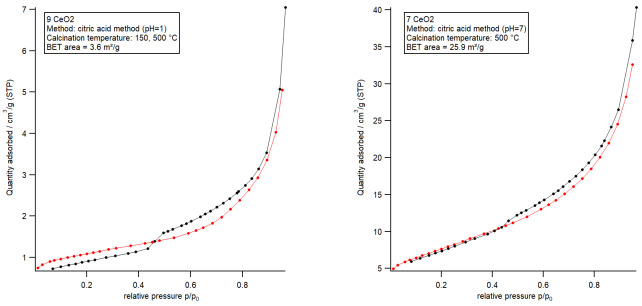

(d) 9 CeO_2-CA1-F500 **(e)** 7 CeO_2-CA7-F500

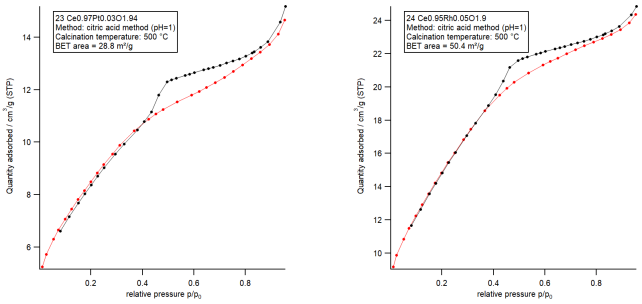

(f) 23 C97PO-CA1-F500 **(g)** 24 C95RO-CA1-F500

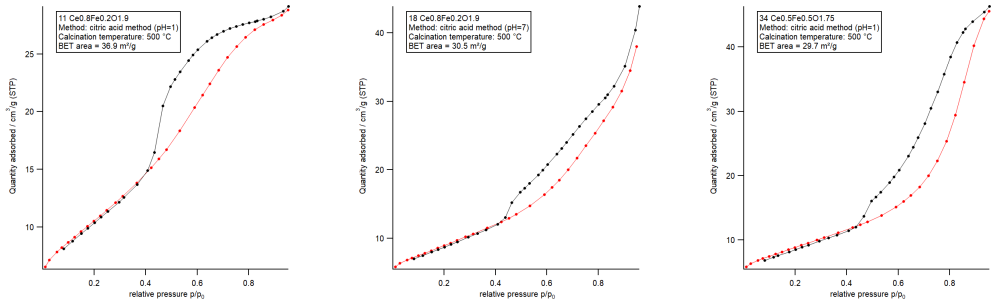

(h) 11 C80FO-CA1-F500 **(i)** 18 C80FO-CA7-F500 **(j)** 34 C50FO-CA1-F500

Figure A.8: Isotherms for citric acid method samples

A.2.5 Modified Pechini method

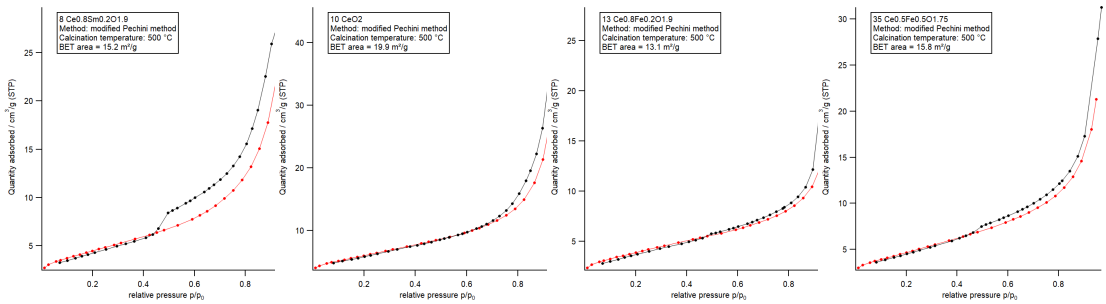

(a) 8 C80SO-PP-F500 **(b)** 10 CeO_2-PP-F500 **(c)** 13 C50FO-PP-F500 **(d)** 35 C50FO-PP-F500

Figure A.9: Isotherms for modified Pechini method samples

A.3 Mass spectrometry plots

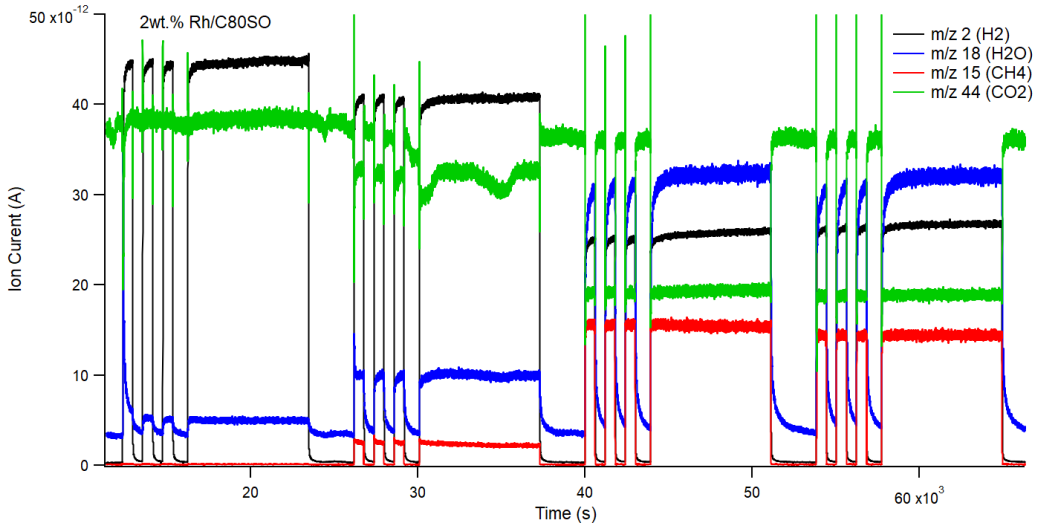

(a) 2 wt.% Rh/C80SO

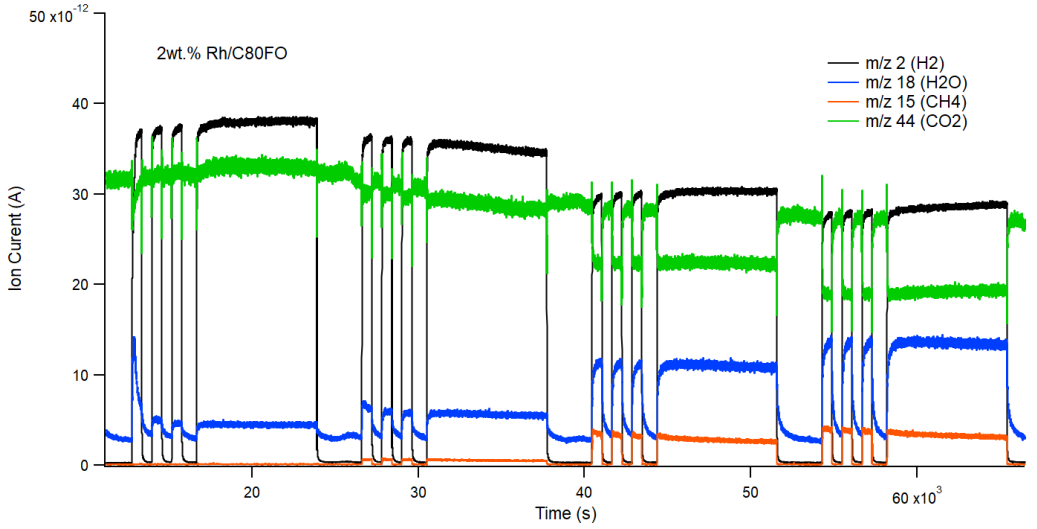

(b) 2 wt.% Rh/C80FO

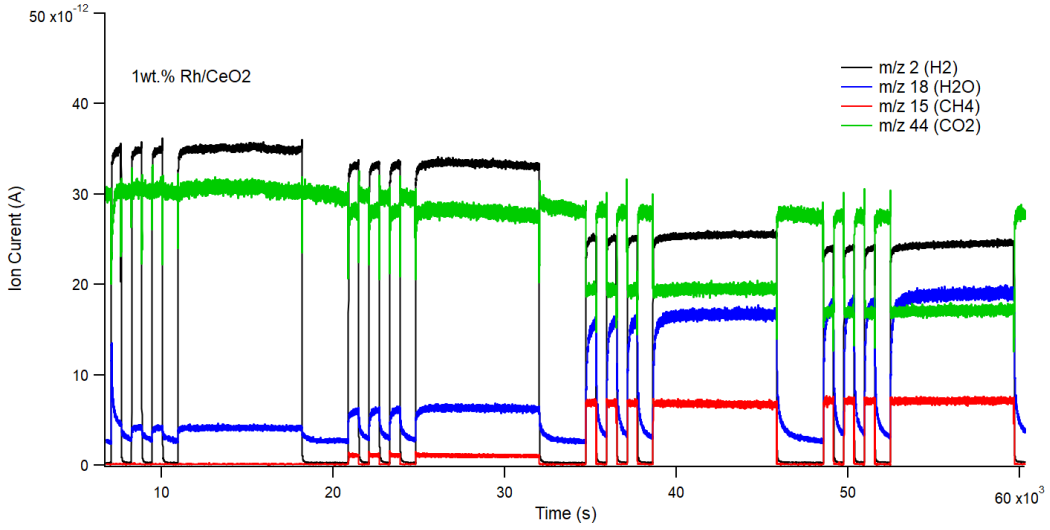

(c) 1 wt.% Rh/CeO2

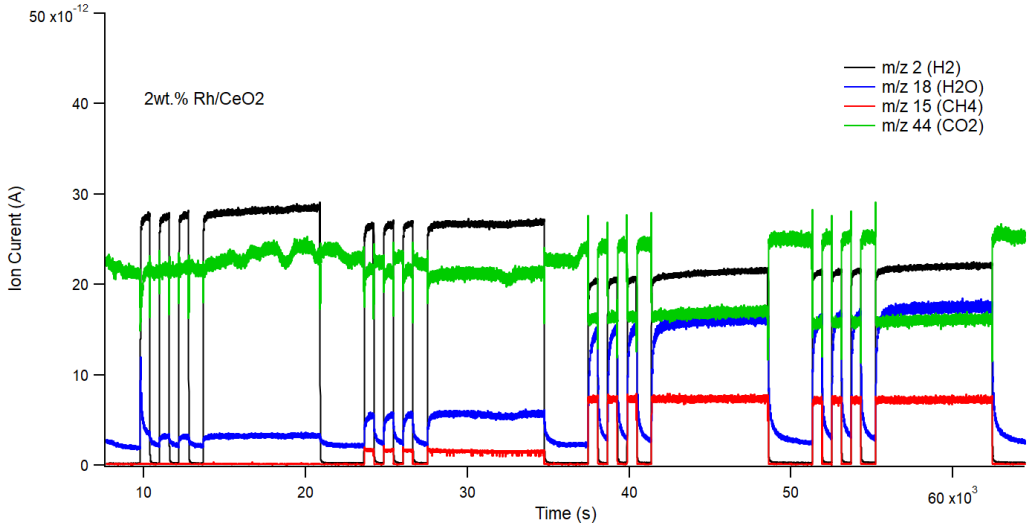

(a) 2 wt.% Rh/CeO2

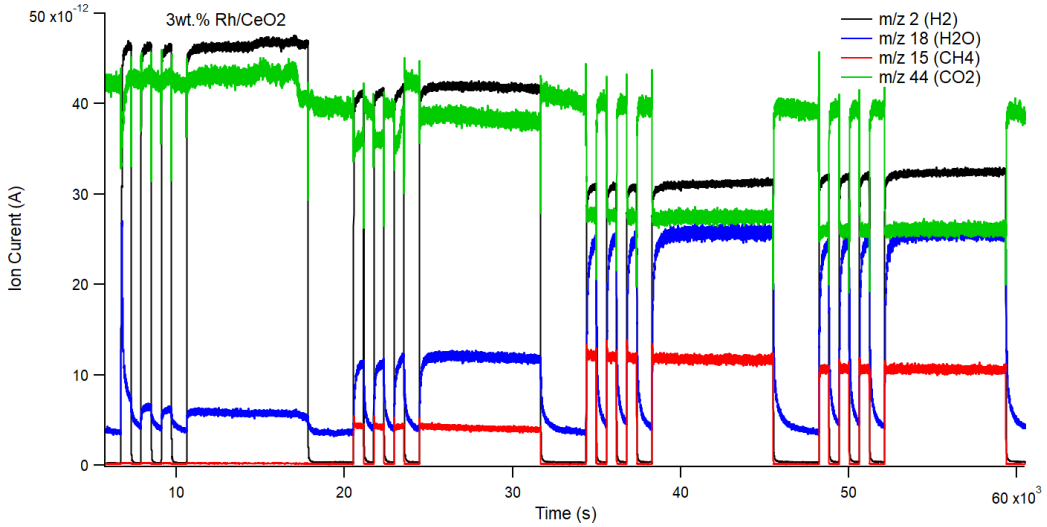

(b) 3 wt.% Rh/CeO2

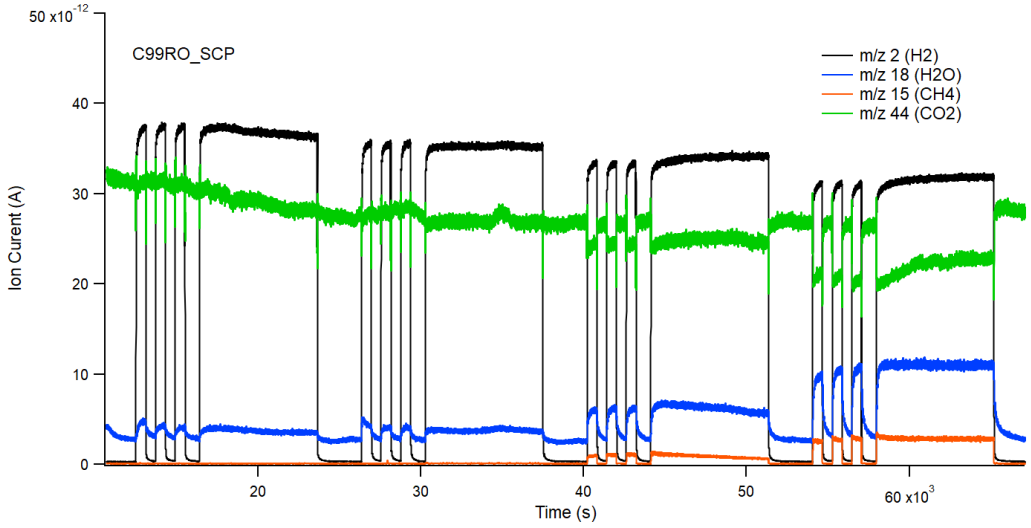

(c) C99RO-SCP

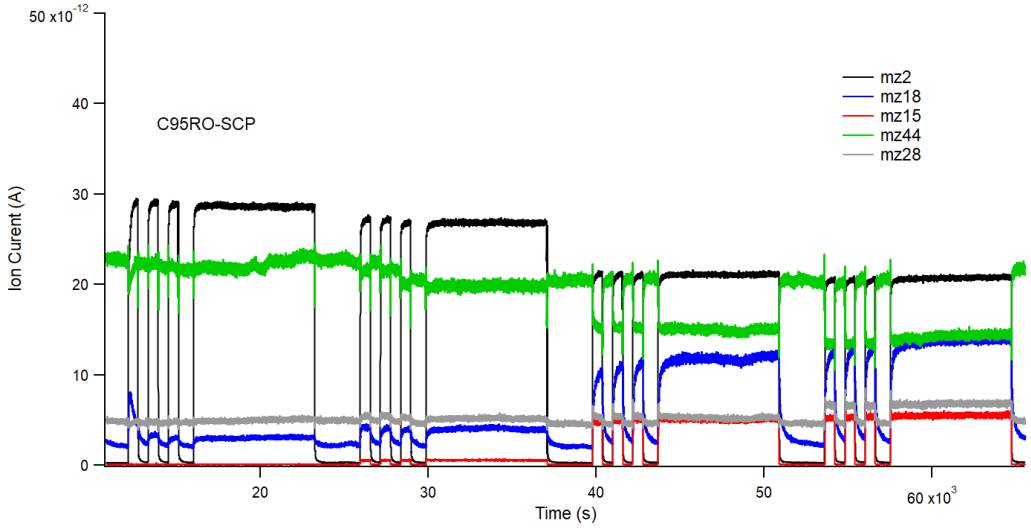

(a) C95RO-SCP

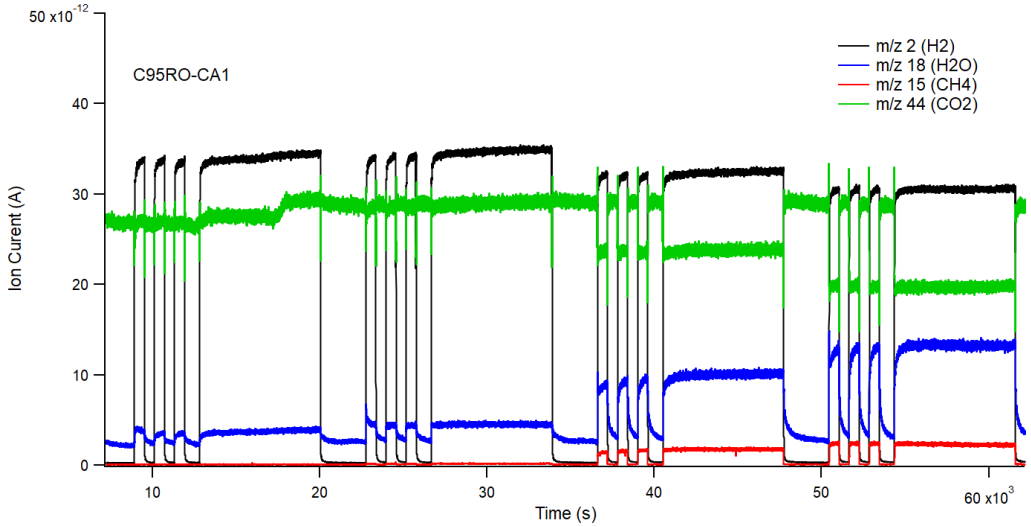

(b) C95RO-CA1

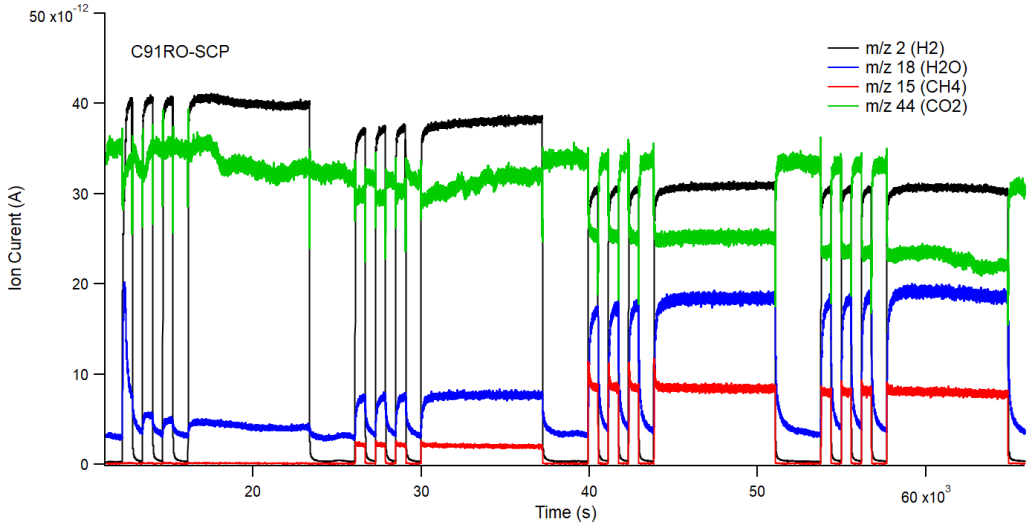

(c) C91RO-SCP

Figure A.12: Mass spectrometry plots for catalysts

DEPARTMENT OF CHEMISTRY AND CHEMICAL ENGINEERING
CHALMERS UNIVERSITY OF TECHNOLOGY
Gothenburg, Sweden
www.chalmers.se

CHALMERS
UNIVERSITY OF TECHNOLOGY